NASA Contractor Report 4753

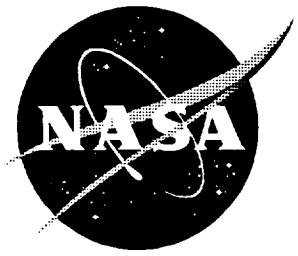

Aeroelastic Calculations Using CFD for a Typical Business Jet Model

Michael D. Gibbons

Contract NAS1-19000
Prepared for Langley Research Center

September 1996

NASA Contractor Report 4753

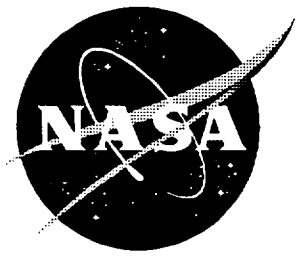

Aeroelastic Calculations Using CFD for a Typical Business Jet Model

Michael D. Gibbons
Lockheed Martin Engineering & Sciences Company • Hampton, Virginia

National Aeronautics and Space Administration
Langley Research Center • Hampton, Virginia 23681-0001

Prepared for Langley Research Center
under Contract NAS1-19000

September 1996

Printed copies available from the following:

NASA Center for AeroSpace Information
800 Elkridge Landing Road
Linthicum Heights, MD 21090-2934
(301) 621-0390

National Technical Information Service (NTIS)
5285 Port Royal Road
Springfield, VA 22161-2171
(703) 487-4650

Aeroelastic Calculations Using CFD for a Typical Business Jet Model

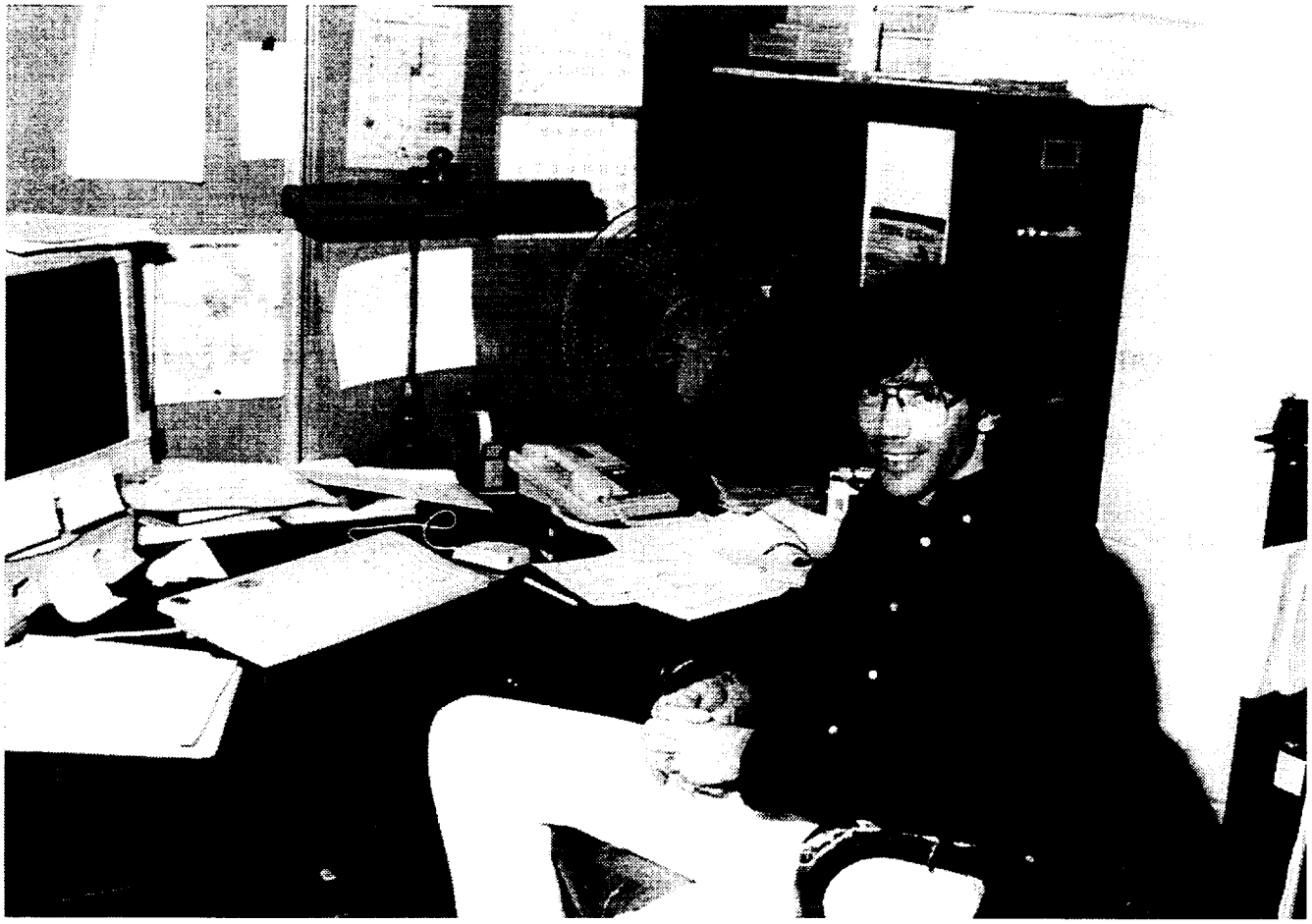

In Memoriam

Michael D. Gibbons

(1960 — 1994)

This report is being published posthumously and is dedicated to the author, Michael D. Gibbons. It should be noted that this report was not complete at the time of Mike's death. He had mentioned to several of his co-workers that he had gathered all of the information necessary to complete the report, but obviously had not had time to process and incorporate all of the data. Mike was a meticulous note-taker, and so with very little effort, we were able to find and extract the necessary information to complete and publish this valuable, well-presented, research. This report stands as a testament to the accuracy, attention to detail, and overall thoroughness Mike applied to all facets of his work.

In the fall of 1994, Mike's Lockheed and NASA co-workers had resigned themselves to the fact that their day-to-day relationship with him was about to change drastically, since he had recently accepted a position with Boeing in Seattle, Washington. Nobody truly felt Mike was leaving since he would always be a phone call, or as he preferred, an e-mail message away. Everyone was excited for him and preparing to offer their best-wishes and farewells when he tragically died just two days before his scheduled departure.

Mike dedicated virtually his entire career to aeroelastic analysis and the prediction of flutter. He was responsible for the development and verification of many of the flutter prediction techniques using computational fluid dynamics in practice today. His work in the application of Transonic Small Disturbance (TSD) potential flow methods to problems in aeroelasticity is unsurpassed. Due to this work, he had established himself as one of the premier computational aeroelasticians in the industry. The research discussed in this report breaks ground in several different areas. From a numerical standpoint, it is a comprehensive study of the impact of varying equation accuracy on unsteady aerodynamic and aeroelastic simulations. Data are presented and compared using methods ranging from linear theory to TSD to full Euler/Navier-Stokes formulations. Second, and more importantly, it provides valuable insight into the role of viscous effects in flutter, especially in the vicinity of the "transonic dip."

This effort was basically Mike's first foray into the world of Euler/Navier-Stokes aerodynamics and its application to aeroelastic problems. As evidenced by this report, it is obvious that he possessed the talent, willingness and dedication required to excel in this field, and the industry will miss him dearly.

To many of us, Mike was a loyal friend who cheered us with his kindness and warm smile. He touched us deeply, and along with his family, we grieve his untimely death. We will always have those happy memories of working and playing with this special friend. His passing has left not only a technical void in the Langley community, but an emotional one as well.

Aeroelastic Calculations Using CFD for a Typical Business Jet Model

Michael D. Gibbons
Lockheed Martin Engineering and Sciences Company

Summary

Two time–accurate Computational Fluid Dynamics (CFD) codes were used to compute several flutter points of a typical business jet wind tunnel model. The model consisted of a rigid fuselage with a flexible semispan wing and was tested in the Transonic Dynamics Tunnel at NASA Langley Research Center where experimental flutter data were obtained from M_∞=0.628 to M_∞=0.888. The computational results were computed using CFD codes based on the inviscid TSD equation (CAP-TSD) and the Euler/Navier-Stokes equations (CFL3D-AE). Comparisons are made between analytical results and with experiment where appropriate. The results presented here show that the Navier-Stokes method is required near the transonic dip due to the strong viscous effects while the TSD and Euler methods used here provide good results at the lower Mach numbers.

Nomenclature

c	local chord
c_r	root chord (1.8942 ft)
c_t	tip chord (0.5433 ft)
C	damping matrix
c_ℓ	sectional lift coefficient
C_p	pressure coefficient
f, Hz.	frequency
f_i	mode shapes (i=1, 6)
K	stiffness matrix
m	mass of wing (0.56522 Slugs)
M	mass matrix
M_∞	freestream Mach number
q_i	generalized displacements (i=1, 6)
q_∞	freestream dynamic pressure
Q	generalized forces
s	semi-span of wing (4.0392 ft)

t	nondimensional time
U_f	flutter velocity
V	volume of truncated cone that encloses wing (5.1945 ft^3)
V_f	flutter speed index $\frac{2U_f}{c_r\omega_3\sqrt{\mu}}$
x,y,z	nondimensional cartesian coordinates
γ	ratio of specific heats
μ	mass ratio
ρ_f	flutter density
ϕ	small disturbance potential
ω_f	flutter frequency, rad./sec.
ω_i	modal frequencies (i=1, 6), rad./sec.

Introduction

Several years ago a significant effort was devoted to the development of a Computational Fluid Dynamics (CFD) method that solves the inviscid Transonic Small Disturbance (TSD) equation for use in aeroelastic analysis. This work was undertaken in order to provide an alternative to the widely used linear methods, such as doublet lattice, and to improve upon previous TSD codes. The code developed to solve the TSD equation is called CAP-TSD[1, 2] and allows transonic effects to be included in flutter calculations. Subsequent to the CAP-TSD effort, a version of CFL3D[3, 4] which solves the Euler/Navier-Stokes equations was modified to allow dynamic aeroelastic calculations.[5] This version of the code is known as CFL3D-AE, and it was used to compute all of the Euler/Navier-Stokes calculations presented in this report. The advantage of using the Euler/Navier-Stokes equations is the improved accuracy in modeling the flow physics. Both CAP-TSD and CFL3D were developed at NASA Langley Research Center.

The purpose of this report is to further assess the above CFD methods for transonic flutter applications. Previously CAP-TSD has been used to compute the flutter boundary of various wings, including thin highly swept delta wings,[6, 7] the AGARD 445.6 wing,[8] and an Active Flexible Wing.[9] CFL3D has been used to solve the Euler[10] and the Navier-Stokes[11] equations for the AGARD 445.6 wing. This report presents results for a typical business jet configuration[12] that was tested in the Transonic Dynamics Tunnel at NASA Langley Research Center. The results include spatial and temporal convergence studies, surface pressure coefficient comparisons for rigid and statically deformed cases, and a discussion of the aeroelastic results using the TSD, Euler, and Navier-Stokes methods.

Numerical Method

This section gives a brief description of the methods used to numerically solve the TSD, Euler/Navier-Stokes, and aeroelastic equations as contained in the CAP-TSD and CFL3D computer codes, respectively.

The CAP-TSD code solves the unsteady transonic small disturbance equation using an implicit time-accurate approximate factorization algorithm with the optional use of internal subiterations to minimize linearization and factorization errors. The unsteady aerodynamics are simultaneously integrated in time along with the structural equations of motion, which allows a time history of the structural response to some initial conditions to be studied. The structure is modeled as a series of orthogonal mode shapes weighted by time varying coefficients known as the generalized displacements. Since the modal deflections in the streamwise and spanwise directions are small in comparison to the vertical modal displacements, they are neglected and the position of the wing at any point in time can be given by

$$z(x,y,t) = \sum_{i}^{modes} q_i(t) f_i(x,y)$$

where q_i is the time varying generalized displacements and f_i represents the vertical components of the mode shapes. This allows the structural equations of motion to be written in generalized coordinates

$$[M]\{\ddot{q}\} + [C]\{\dot{q}\} + [K]\{q\} = \{Q\}$$

where [M], [C], and [K] are the generalized mass, damping and stiffness matrices and $\{Q\}$ is the generalized aerodynamic forces. The unsteady aerodynamics can be computed using different forms of the TSD equation by choosing different coefficients. Two different forms of the TSD equation were used here by choosing either the linear equation coefficients or the so-called AMES coefficients. The linear results were computed using the form

$$\begin{aligned}
&\frac{\partial}{\partial t}\left(-M_\infty^2\phi_t - 2M_\infty^2\phi_x\right) \\
&+ \frac{\partial}{\partial x}\left(\left(1 - M_\infty^2\right)\phi_x\right) \\
&+ \frac{\partial}{\partial y}(\phi_y) \\
&+ \frac{\partial}{\partial z}(\phi_z) = 0
\end{aligned}$$

The nonlinear results were computed using the TSD equation written using the AMES coefficients given by

$$\frac{\partial}{\partial t}(-M_\infty^2\phi_t - 2M_\infty^2\phi_x)$$
$$+\frac{\partial}{\partial x}\left((1-M_\infty^2)\phi_x - \frac{1}{2}(\gamma+1)M_\infty^2\phi_x^2 + \frac{1}{2}(\gamma-3)M_\infty^2\phi_y^2\right)$$
$$+\frac{\partial}{\partial y}(\phi_y(1-(\gamma-1)M_\infty^2\phi_x))$$
$$+\frac{\partial}{\partial z}(\phi_z) = 0$$

When the linear equation was used, the wing was modeled as a flat plate in order to produce results similar to other linear methods such as doublet lattice. When the nonlinear equation was used, the wing was modeled using the appropriate airfoil shapes so that nonlinear effects (such as moving shock waves) could be modeled. All CAP-TSD calculations included the effects of shock generated entropy and vorticity.[13] The linear pressure coefficient equation was used to compute the surface pressure values. Version 1.3 of CAP-TSD was used in all calculations.

The CFL3D code solves either the Euler or Navier-Stokes equations using an implicit time-accurate approximate factorization algorithm involving either flux vector splitting or flux difference splitting. For the calculations presented here, flux-vector splitting was used. For the Navier-Stokes calculations, turbulence was modeled using the Baldwin-Lomax model. Coupling of the structural equations of motion with the aerodynamics was done similar to that implemented in CAP-TSD. As with CAP-TSD, only the vertical component of the mode shape is used.

Aeroelastic Calculations for a Typical Business Jet

This section discusses the numerical results obtained for a business jet configuration. Details of the geometry and the CFD models used in the calculations are included. Every attempt was made to verify the spatial and temporal convergence of the solutions. Results are presented which show the convergence of selected cases. Sensitivity of the aeroelastic solutions to the initial conditions are also presented. Surface pressure comparisons are made for the static rigid and static aeroelastic cases. Finally, dynamic aeroelastic results are presented using different equation levels, and comparisons are made with experimental data.

Model Geometry

The business jet configuration consisted of a semispan wing/fuselage configuration which was tested in the Transonic Dynamics Tunnel (TDT) at NASA Langley Research Center. Figure 1 shows an illustration of this model mounted on the wall of the TDT. The model was tested in air for a range of freestream Mach

numbers to obtain flutter points. The model, however, was not instrumented to measure surface pressure data. Experimental flutter data were obtained for Mach numbers ranging from 0.628 to 0.888[14]. The wing root angle-of-attack was varied during the test to minimize loading with the maximum angle needed for this purpose being 0.2 degrees. The wing has a taper ratio of 0.29 and a midchord sweep of 23 degrees. The airfoil thickness varies from 13 percent at the symmetry plane (for the extended wing configuration) to 8.5 percent at the wing tip. The fuselage has a circular cross-section with a conical aft end.

The CAP-TSD calculations for the wing/fuselage configuration involved a 100x50x80 point computational grid with 45 points along the chord of the wing and 25 points along the span. Figure 2 shows a perspective view of the wing/fuselage surface grid. Figure 3 shows the four airfoil sections used to define the wing surface. Linear interpolation is used to define the airfoil sections at other spanwise locations. Calculations were also performed for a wing alone configuration to study the effect of the fuselage on the results. Calculations for the wing alone used the same grid as the wing/fuselage configuration but with the wing extended to the symmetry plane.

Figure 4 shows the mode shapes for the wing, and Table 1 gives the generalized masses and frequencies used in the aeroelastic calculations. The mode shapes and generalized masses were computed from a finite element structural model using NASTRAN. The frequencies are experimental values measured during testing of the model in the TDT. As with most models of this type, a yaw mode is present which includes very small vertical displacements. In all subsequent analyses, this yaw mode is neglected and is not shown in the above figure.

The CFL3D calculations for the extended wing were made primarily with two grids as shown in Figures 5 and 6. The Euler mesh contained 153 points around the airfoil and wake, 57 points out the span with some clustering around the wing tip, and 33 points normal to the wing surface. There were 113 points around each airfoil section and 41 points on the wing spanwise. The Navier-Stokes mesh was virtually identical except there were 51 points normal to the wing. Both meshes used a C-H topology. No attempt was made to model the fuselage since inviscid TSD results showed that it has little effect on the flutter solution as discussed later. Viscous interactions between the wing and fuselage could impact flutter results, but detailed analyses of these types of interactions are beyond the scope of this effort.

Spatial and Temporal Convergence

Prior to making numerous aeroelastic calculations, a convergence study was done with CAP-TSD and the CFL3D-Euler results. The effect of time step on the CAP-TSD solutions is shown using the linear and nonlinear equations, and the effect of grid density is shown for a case using the nonlinear equation. Spatial and temporal convergence of the CFL3D-Euler results are shown. No

convergence study was done using the CFL3D-Navier-Stokes version due to the large computational time required. By making these calculations, a grid density and time step were chosen which produced solutions of acceptable accuracy and yet require the minimum amount of computer time.

CAP-TSD

The temporal convergence study was performed at M_∞=0.6 with CAP-TSD using the nonlinear equation and at M_∞=0.9 using the linear and nonlinear equation. Table 2 shows the effect of time step on the predicted flutter dynamic pressure at M_∞=0.9 using the linear TSD equation. The table shows the flutter dynamic pressure and frequency computed using a time step based on 165, 330, and 660 steps per cycle of motion in the third modal frequency (31.6 Hz). Increasing the number of time steps from 165 to 330 results in roughly a 7 percent reduction in predicted flutter dynamic pressure whereas increasing from 330 to 660 only produces about a 1 percent reduction in flutter dynamic pressure. Figure 7 shows the first generalized displacement computed at M_∞=0.6 using the exact same input files except for the time step. The figure shows the large error when the solution is not converged temporally. Using a time step of 0.1 results in an unstable structural response whereas a value of 0.0339 produces a stable structural response. Reducing the time step further to 0.0166 resulted in no significant change from the response at 0.0339. The nonlinear case at M_∞=0.9 is shown in Figure 8. The transients shown correspond to 330 and 660 steps per cycle of motion. Figure 8 indicates that at M_∞=0.9 a temporally converged solution was obtained when using 330 steps/cycle. The time step used in the remaining unsteady calculations was based on 330 steps per cycle of motion since the increased accuracy at 660 was deemed minimal.

A spatial convergence study for a nonlinear case at M_∞=0.9 and q_∞=21.6 psf is shown in Figure 9 using two different grid densities. The first grid size was 100x50x80 and is used in all the other results computed in this paper; the second grid size was 140x70x90. The second grid has 60 points along the chord and 35 points along the span with clustering near the wing tip. Figure 9 shows that the two solutions are nearly identical. This good comparison suggests that the 100x50x80 grid produces solutions of acceptable spatial accuracy.

CFL3D-Euler

Three different grid densities were used to study spatial convergence of the CFL3D-Euler solution at M_∞=0.9 and zero degrees angle of attack. The grids used were constructed using a C-H topology. These grids contained 153x43x33, 153x57x33, and 263x57x33 grid points. The index refers to the number of points around the airfoil chord, spanwise, and normal to the surface, respectively. Figure 10 shows the comparisons between the three solutions. Each grid gives nearly the same solution with the spanwise index having the greatest influence on the

location of the upper surface shock near the wing tip, and the chordwise index affecting the resolution of a small lower surface shock near the tip. Based on these calculations, the 153x57x33 grid was selected as producing a solution with an acceptable level of spatial accuracy for the aeroelastic calculations presented in this report.

The CFL3D-Euler calculations used a time step of 0.05 for all the unsteady results presented. To determine how sensitive the solutions were to time step, a calculation was done with a time step of 0.01 for an aeroelastic case at M_∞=0.9 and q_∞=36.0 psf. Figure 11 shows a plot of the first generalized displacement for the two different time steps. Since the two solutions are nearly identical, the larger time step of 0.05 was used for further dynamic aeroelastic calculations.

Initial Conditions

Each dynamic aeroelastic calculation is computed by using the converged static aeroelastic solution with some form of initial condition prescribed for the generalized displacements or velocities of each structural mode. Typically, the initial condition on the generalized displacements of each mode is taken to be zero which should help to reduce numerical transients which otherwise might be created by the wing instantaneously being displaced. To initiate the motion of the wing, the generalized velocities of each mode have been set to 1.0 in all the dynamic aeroelastic calculations presented unless noted otherwise. By setting all of the generalized velocities to 1.0 (ie, $\dot{q}_i = 1.0, i = 1, 6$), each mode actively participates in the structural response. This allows for accurate values of damping and frequency to be extracted from each generalized displacement.

The choice of using an initial generalized velocity of 1.0 is somewhat arbitrary and its effect on the structural response depends on how the mode shapes were scaled. To show the effect that different values have on the solution, values of 0.1, 1.0, and 10.0 were used as initial conditions at M_∞=0.85, q_∞=64.8 psf for the wing/fuselage configuration. These calculations were done using the CAP-TSD code. Figure 12 shows the structural response of the first generalized displacement. Each response was normalized by the initial condition amplitude for direct comparison. Figure 12 indicates that the responses are quite similar, and when damping and frequency information is extracted from each curve, the frequency values are nearly identical, as shown in Table 3, while the damping values range within five percent of each other. The amplitude of motion at the wing tip leading edge caused by the different initial conditions varied from a maximum of +/– 0.015 degrees to +/– 1.5 degrees for the initial conditions 0.1 and 10.0, respectively. These calculations indicate the aeroelastic response to a set of initial conditions behaves in a linear fashion with the initial conditions even though the mean flow field contains nonlinear features. Similar results were obtained at a higher Mach number, M_∞=0.9, for the wing alone case as shown in Figure 13 and Table 4.

Methodology to Locate Flutter Crossing

To compute the point at which flutter occurs for a given Mach number, several executions of a code are required. First, a static aeroelastic solution is computed using a value of the dynamic pressure that is assumed to be near that which produces flutter (neutral stability). Next, a dynamic aeroelastic solution is computed by restarting the calculation from the converged static aeroelastic solution with some initial condition on the vertical velocity of the wing. The generalized displacements from the dynamic case are fit with a series of exponentially damped sine waves[15] allowing the stability of the system to be determined. If the aeroelastic solution was stable, a higher value for the dynamic pressure is chosen and the static and dynamic aeroelastic solutions are again computed. Once two or more transients have been computed, the flutter dynamic pressure value is determined by linear extrapolation using the damping information from the curve fitting process. Linear extrapolation or interpolation gives an estimate of the conditions that produce flutter. However, further refinement can be obtained by additional aeroelastic calculations if improved accuracy is desired.

An alternative method to calculate the flutter crossing is to vary free stream velocity while holding density constant (usually to the experimental flutter density). This approach allows the mass ratio of the calculation to match the experimental value. Since this method generally requires that the flutter solution be known before it is computed, the method of varying density is generally used. An additional reason to vary density rather than velocity is that the flutter dynamic pressure is generally more sensitive to changes in density than velocity thus making it easier to determine the point of neutral stability.

Static Rigid Results

In this section, comparisons of the surface pressure coefficients computed with CAP-TSD and CFL3D are shown for the extended wing at zero degrees angle of attack. Due to the lack of experimentally measured surface pressures, comparisons are made between different codes. The most direct comparison to make with CAP-TSD is the CFL3D-Euler results since both methods assume the flow to be inviscid. Comparisons between CFL3D-Euler and CFL3D-Navier-Stokes generated surface pressure distributions are shown to indicate the effect that viscosity has on the steady solution. These calculations were made for the extended wing configuration only since the fuselage was not modeled in the CFL3D calculations.

Comparisons between CAP-TSD and CFL3D-Euler surface pressure coefficients are shown for M_∞=0.7 and M_∞=0.9 at zero degrees angle of attack. Figures 14 and 15 show that CAP-TSD compares favorably with the CFL3D-Euler results. At M_∞=0.7, both methods are in excellent agreement for this subsonic case. When the Mach number is increased to 0.9, a shock wave develops along the upper surface with a weaker shock wave on the lower surface. Comparisons between

the two methods indicate a slight difference in the surface pressure magnitude at some span stations. On the lower surface near midspan, CAP-TSD predicts the shock is located further upstream than the Euler results. Part of this difference may be due to the CAP-TSD grid which had a finer spacing in the spanwise direction near the wing root than the Euler grid did. Although not shown, additional CAP-TSD calculations with a finer spacing at the wing trailing edge, resulted in excellent comparisons of the surface pressure coefficients near the wing trailing edge but the refinement had little effect on the overall surface pressures.

Comparisons are also shown between the sectional lift coefficients for the above two cases in Figure 16. As expected, the comparison between CAP-TSD and CFL3D is fairly good at M_∞=0.7 but shows some significant differences at M_∞=0.9. These differences are due to the slight disagreement in the surface pressures shown in Figure 15.

To show the effect that viscosity has on the position and strength of the shock waves, a comparison was made between the CFL3D-Euler and CFL3D-Navier-Stokes results at M_∞=0.9, zero degrees angle of attack, and Re = 1.107×10^6. This Reynolds number is typical of the value obtained during flutter tests this model in the TDT. Figure 17 shows how the shock on the upper surface is significantly weakened and shifted forward. The rapid recompression at the trailing edge is also weakened due to the presence of the boundary layer. Aeroelastically, the most important features are the forward shift in the shock resulting in a forward shift in the aerodynamic center and the lower loads experienced on the wing due to the weakening of the shock.

Static Aeroelastic Results

Prior to making a dynamic aeroelastic calculation, the wing was allowed to deform due to the static air loads. To obtain a converged static aeroelastic solution, six normal modes were used. A structural damping value of 0.99 (nearly critically damped) was used for each mode while the solution was marched in time. Surface pressure distributions are shown, and comparisons are made between CAP-TSD and CFL3D-Euler results. The aerodynamic center and its relationship to the first torsion node line, based on CAP-TSD calculations, are also plotted.

Figure 18 shows a three dimensional view of the upper and lower surface pressure coefficients computed with CAP-TSD for the wing/fuselage configuration. Results are shown at M_∞=0.8, 0.85, 0.9, and 0.95 for the converged static aeroelastic deflections near the flutter dynamic pressure. These figures show the development of strong shocks on the surface of the wing. At M_∞=0.95, the upper and lower surface shock has reached the trailing edge with the recompression occurring slightly downstream of the wing trailing edge. The occurrence of a shock near the wing root trailing edge is due to the aft shape of the fuselage which results in a rapid expansion followed by a shock. As Figure 2 shows, the fuselage becomes conical at approximately eight tenths root chord. Figure 18 shows that

the shock completely disappears when the aft end of the fuselage was replaced by a cylinder extending to the downstream boundary. In reality, the development of such strong shocks may not occur due to the effect of viscosity which tends to weaken shocks and move them forward.

Comparisons between the CAP-TSD and CFL3D-Euler static aeroelastic solutions at M_∞=0.7 and M_∞=0.9 are shown in Figures 19 and 20. At M_∞=0.7 and q_∞=115.2 psf, comparisons between the CAP-TSD and CFL3D-Euler results are quite good. At this Mach number a strong suction peak exists along the lower surface leading edge. This is due to the negative effective angle of attack produced by the twist of the deformed wing.

At M_∞=0.9 and q_∞=36.0 psf, comparisons between CAP-TSD and CFL3D-Euler pressures (Figure 20) are good. However, CAP-TSD predicts the lower surface shock wave to be located further forward near the wing tip than predicted by CFL3D. Part of the difference in the solutions is due to the statically deformed shape. The loading predicted with CAP-TSD results in the wing tip leading edge being deflected 1.81 degrees nose down whereas CFL3D-Euler predicts a deflection of 1.74 degrees. Since the loads on the wing were slightly different for the rigid case, the resulting static aeroelastic shape must be different.

A comparison of the sectional lift at M_∞=0.7 and M_∞=0.9 is shown in Figure 21. At M_∞=0.7, the comparison between CAP-TSD and CFL3D sectional lift is fairly good with some discrepancy near the wing tip. At the higher Mach number of M_∞=0.9, CAP-TSD tends to predict a higher loading at the wing tip and a lower loading at wing root again due in part to the difference in the statically deformed shape.

Figure 22 shows how the aerodynamic center, computed with CAP-TSD near the flutter dynamic pressure, varies as the Mach number increases from M_∞=0.7 to M_∞=0.9. At M_∞=0.7, the aerodynamic center is located well forward of the first torsion node line near the quarter chord line as expected. This is one reason why subsonically a higher dynamic pressure is required to produce flutter. As the Mach number increases, the aerodynamic center moves aft and at M_∞=0.9 lies close to the first torsion node line. This reduces the aerodynamic damping of the wing. With less damping the dynamic pressure which will produce flutter is expected to decrease. Although not shown, calculations where the dynamic pressure was varied at a constant Mach number indicated little change in the location of the aerodynamic center.

Dynamic Aeroelastic Results

The flow conditions which produce flutter that are presented in this section were computed using TSD, Euler and the Navier-Stokes equations. Calculations for the wing/fuselage configuration and the extended wing configuration were made with CAP-TSD. Since the presence of the fuselage appeared to have little effect on the aeroelastic solutions, the Euler and Navier-Stokes calculations were

made only for the extended wing. Calculations are presented to show the effect of the fuselage, mass ratio, and equation level.

For each calculation the results were tabulated and plotted. To eliminate any possible confusion on how certain quantities were calculated, the expressions used are given here. The mass ratio was computed using

$$\mu = \frac{\mathrm{m}}{\mathrm{V}\rho_f}$$

where

$$\mathrm{V} = \frac{1}{12}\pi s\left(c_t^2 + c_t c_r + c_r^2\right)$$

and 'm' is the mass of the wing, 's' is the semispan of the wing, 'c_t' is the tip chord, and 'c_r' is the root chord at the wing fuselage intersection. The subscript on density refers to the value at flutter. The reduced frequency was computed using

$$\mathrm{k} = \frac{\mathrm{c_r}\omega_\mathrm{f}}{2\mathrm{U_f}}$$

where ω_f is the flutter oscillatory frequency, and $\mathrm{U_f}$ is the flutter free stream speed. The flutter speed index was computed using

$$\mathrm{V_f} = \frac{2\mathrm{U_f}}{\mathrm{c_r}\omega_3\sqrt{\mu}}$$

where ω_3 is the third modal frequency corresponding to first torsion.

CAP-TSD results

Several flutter points were computed with CAP-TSD using the linear and nonlinear equations. For both sets of results, the flutter points were computed by holding velocity constant and varying density unless stated otherwise. No structural damping was used in these calculations. All calculations were performed with the wing root set at zero degrees angle of attack. Each dynamic aeroelastic calculation was restarted from a converged static aeroelastic solution. The majority of the unsteady calculations were computed using 330 steps per cycle of the third modal frequency. Typical CPU execution times were 3.1 micro seconds per grid point per time step on a CRAY 2. Flutter data for the business jet wing are tabulated in Tables 5 through 13. Experimental data obtained in the NASA Langley Research Center Transonic Dynamics Tunnel are presented in Table 5 for comparison with the following computed results.

Figure 23 (Table 6) shows that the CAP-TSD linear results for the wing/fuselage configuration at low Mach number are in excellent agreement with the experimental results. The good agreement between CAP-TSD linear results and experiment at the lower Mach numbers should be expected since nonlinear aerodynamic effects are insignificant whereas linear theory is thought to give reasonable answers at higher Mach numbers due to the counteracting effects of

thickness and viscosity. Thickness has a destabilizing effect at transonic speeds for inviscid flows whereas viscosity tends to be stabilizing. A comparison between the CAP-TSD results computed with the linear (Table 6) and nonlinear (Table 7) equation in Figure 23 show that thickness has a significant effect above M_∞=0.7. The large differences between the results using the linear and nonlinear equations are due to the presence of strong shocks in the flow field.

For the results computed with the nonlinear equation, calculations at M_∞=0.9 indicated a very low dynamic pressure may have been needed to obtain a flutter crossing. At this Mach number all solutions computed by varying density down to a dynamic pressure of 7.2 psf were unstable with low damping. Since such an unrealistically low dynamic pressure may have been needed to obtain a flutter crossing no point was plotted for this case.

The effect of the fuselage on the flutter results is shown by two calculations in which the fuselage was removed and the wing extended to the symmetry plane. Results of this analysis are tabulated in Table 8. As shown in Figure 24, the effect of the fuselage is minimal. This is expected since the generalized aerodynamic forces are weighted by the mode shapes, and near the root where the interference effects of the fuselage are greatest, the modal displacements are nearly zero thus resulting in a contribution to the generalized aerodynamic forces which is far smaller than the contributions from the loading near the wing tip where the modal displacements are greatest.

Figure 25 (Table 9) shows the effect of matching the mass ratio to the experimental value. These calculations are done by holding density constant at a linear extrapolation of the experimental density and varying both dynamic pressure and velocity. At M_∞=0.8, there is no significant difference between the calculations which match velocity or density. However, at M_∞=0.9, a solid flutter point was obtained with CAP-TSD while the velocity was being varied. This is in contrast to the unstable solutions computed by varying density while holding velocity constant. Based on the improved solutions computed by varying velocity, one should not conclude that this provides more accurate answers than varying density. Varying velocity effectively changes the phase lag, which has been pointed out by Zwann[16] as being a primary cause of the transonic dip. Thus, if the theoretical flutter velocity is significantly different from the experimental velocity, the flow physics may not be the same as those in the experimental data making direct comparisons meaningless. This implies the velocity should be held fixed at the experimental value; however, a somewhat different argument might be made for varying density which affects wing loading.

Figure 26 provides further insight into the inviscid flutter by showing the modal interactions for the previous CAP-TSD results computed with the nonlinear equation for the wing/fuselage configuration in root locus form. These figures show frequency versus damping for each mode with stable roots on the left and unstable roots on the right of each of the figures. In Figures 26a, 26b, and 26c, the mode which first becomes unstable is first bending. These results are very similar

to those obtained by Mohr, Batina, and Yang[17] who show a study of the flutter mechanism for a wing similar to the one studied here. In Reference [17] however, the mass ratio was held constant, whereas in the present study, the mass ratio was allowed to vary with increasing Mach number. Calculations with CAP-TSD at lower mass ratios for the M_∞=0.9 case (Table 10) showed that as the mass ratio decreases, the dynamic pressure which produces flutter increases, and the type of mode shift shown in Reference [17] occurs; that is, the first torsion mode appears to be the primary flutter mechanism. With the higher mass ratios encountered for the CAP-TSD calculations varying density, there does not appear to be a shift in the primary flutter mechanism, which remains first bending into supersonic flow. Reference [17] attributes the mode shift to the upper surface shock passing across the first torsion node line. Similar results shown here indicate that as the shock moves aft, there is a reduction in aerodynamic damping due to the aft movement of the aerodynamic center. As the Mach number increases from M_∞=0.7 to M_∞=0.85, the largest stable value of damping gradually decreases with the frequency decreasing for zero damping. The decrease in frequency is also shown in Figure 23b. Further calculations have shown that the third mode eventually goes unstable, but at much higher dynamic pressures. At M_∞=0.9, both the first bending mode and first torsion go unstable and appear to be unstable even at dynamic pressures near zero (large mass ratios).

CFL3D results

The following section presents aeroelastic results which were computed using the Euler and Navier-Stokes equations as solved by CFL3D. These results were computed using the extended wing configuration with no structural damping and with the wing root angle-of-attack at zero degrees. Both the Euler and Navier-Stokes solutions were computed by holding velocity constant and varying density unless stated otherwise. As with the TSD calculations, the dynamic aeroelastic calculations were restarted from a converged static aeroelastic solution. The Euler calculations were made with a 153x57x33 grid while the Navier-Stokes calculations used a 153x57x51 grid. Typical execution times were approximately 46.0 micro seconds per grid point per time step for the Euler calculations and 50.0 micro seconds per grid point per time step for the Navier-Stokes calculations on a CRAY 2.

Figure 27 shows a comparison between Euler (Table 11) and TSD (Table 8) results. The comparison shows that both methods give nearly the same result at M_∞=0.7 and M_∞=0.85. At slightly higher Mach numbers of 0.92 and 0.94, the Euler calculations predict unstable responses down to 7.2 psf similar to the results at M_∞=0.9 computed with CAP-TSD. Apparently, inviscid solutions for this configuration do not contain sufficient aerodynamic damping and result in a free response as the Mach number approaches values around 0.92. Both Euler and TSD calculations performed near this Mach number exhibit very low flutter dynamic pressures, which are not displayed on this plot. As the Mach number is

increased to M_∞=1.05, a clear boundary between stable and unstable aeroelastic transients allowed a flutter point to be computed. An examination of the frequency at flutter indicates a mode shift has occurred which is apparently due to second bending.

Figure 28 shows the effects of mass ratio on the computed flutter points. Since varying velocity while holding density constant had a significant effect on the CAP-TSD solution at M_∞=0.9, this method was used to compute the flutter crossing with CFL3D-Euler (Table 12). As with the CAP-TSD mass ratio results shown in Figure 25, there is little difference in the method used to compute the flutter point below M_∞=0.85. At M_∞=0.9 the method of varying velocity predicts a slightly higher flutter speed index.

The effects of viscosity on the flutter solution are shown in Figure 29. These calculations were computed by holding velocity constant and varying density using the Navier-Stokes equations. Figure 29 compares the Navier-Stokes solutions with the Euler results. Comparisons show that the addition of viscosity results in a small increase in the flutter speed at M_∞=0.85 while at M_∞=0.9 there is a significant increase in the predicted flutter speed index. As the Mach number is increased further to M_∞=0.92, the predicted boundary begins to turn upwards indicating that the transonic dip occurs near M_∞=0.9. The significant difference between the Euler solution at M_∞=0.9, which is effectively at an infinite Reynolds number, and the Navier-Stokes solution indicates the importance that viscosity plays for this configuration. Since the Reynolds number is approximately one million for both the Navier-Stokes calculations and experimental data near M_∞=0.9, it is interesting to note that the experimental data may be nonconservative in comparison to flight tests since they usually occur at Reynolds numbers greater than one million. The Navier-Stokes results presented in Figure 29 are tabulated in Table 13.

Conclusions

Detailed aeroelastic calculations have been presented for a business jet configuration computed using the TSD equation, Euler equations, and the Navier-Stokes equations. The TSD calculations were computed with CAP-TSD while the Euler and Navier-Stokes were computed with CFL3D.

Comparisons with experiment show that CAP-TSD does a fairly good job in predicting the flutter boundary for the business jet model at the lower Mach numbers with the results becoming conservative for the higher Mach numbers. The reason for the discrepancy appears to be due to the inviscid nature of the calculations. Without viscosity, shocks are typically much stronger and further aft resulting in greater loads at a given value of dynamic pressure. Calculation of the flutter points by varying density or velocity showed no significant differences although varying velocity at M_∞=0.9 did allow for a flutter point to be obtained.

Calculations with the Euler equations showed little difference from the CAP-TSD solutions; both methods predicted a rapidly dropping flutter boundary as M_∞=0.9 was approached. Apparently, the assumptions made with TSD, such as small perturbations and irrotational flow, are adequate for these cases. Calculation of the flutter points by varying density or velocity showed no significant differences.

The results computed with the Navier-Stokes equations showed a significant improvement in the comparisons between the computed flutter points and experiment. The remaining differences between experiment and computed values might be further improved by using a turbulence model which models separation such as the Johnson-King turbulence model. Some improvement might also be obtained by using a finer mesh. Other factors affecting the accuracy of the computed flutter points include the accuracy of the structural mode shapes. The structure is generally modeled using a subset of orthogonal mode shapes and an accurate correlation of the computed mode shapes with experimentally measured values may be necessary; if, for instance, the torsion node line near the wing tip were inaccurately predicted, it could result in a completely different pitching moment. Additionally, the structural damping of the wing should be measured and included since the transonic dip region tends to be a region of low aerodynamic damping.

The goal of this report was to further study the use of CFD for predicting flutter. The results presented here indicate that good agreement with experimental data can be obtained with the Navier-Stokes code near the transonic dip. At the lower Mach numbers, the TSD and Euler results show good agreement with experimental data. Comparisons between the various equations levels showed the importance of modeling viscosity near the transonic dip and how it had little effect on the results at the lower Mach numbers. Since different configurations may be more or less sensitive to viscous effects, then obtaining good comparisons with experimental data at a minimum cost (CPU time) requires selecting the appropriate method for the flow conditions.

Bibliography

[1] Batina, J. T., "Efficient Algorithm for Solution of the Unsteady Transonic Small-Disturbance Equation," *Journal of Aircraft*, vol. 25, pp. 598–605, July 1988.

[2] Batina, J. T., "Unsteady Transonic Algorithm Improvements for Realistic Aircraft Applications," *Journal of Aircraft*, vol. 26, pp. 131–139, Feb. 1989.

[3] Anderson, W. K., Thomas, J. L., and Van Leer, B., "Comparison of Finite Volume Flux Vector Splittings for the Euler Equations," *AIAA Journal*, vol. 24, pp. 1453–1460, 1986.

[4] Anderson, W. K., Thomas, J. L., and Rumsey, C. L., "Extension and Application of Flux-Vector Splitting to Unsteady Calculations on Dynamic Meshes," AIAA Paper No. 87–1153, June 1987.

[5] Robinson, B. A., Batina, J. T., and Yang, H. T. Y., "Aeroelastic Analysis of Wings using the Euler Equations with a Deforming Mesh," *Journal of Aircraft*, vol. 28, pp. 781–788, Nov. 1991.

[6] Gibbons, M. D., Soistmann, D. L., and Bennett, R. M., "Flutter Analysis of Highly Swept Delta Wings by Conventional Methods," NASA TM 101530, Nov. 1988.

[7] Soistmann, D. L., and Gibbons, M. D., "Some Analytical Transonic Flutter Calculations of a Highly Swept Delta Wing," NASP CR 1084, May 1990.

[8] Cunningham, H. J., Batina, J. T., and Bennett, R. M., "Modern Wing Flutter Analysis by Computational Fluid Dynamics Methods," *Journal of Aircraft*, vol. 25, pp. 962–968, Oct. 1988.

[9] Silva, W. A., "Investigation of the Aeroelastic Stability of the AFW Wind-Tunnel Model using CAP-TSD," AGARD Structures and Materials Panel Specialists Meeting on Transonic Unsteady Aerodynamics and Aeroelasticity, San Diego, California, Oct. 1991.

[10]Lee-Rausch, E. M., and Batina, J. T., "Wing Flutter Boundary Prediction using Unsteady Euler Aerodynamic Method," AIAA Paper No. 93–1422, Apr. 19-21 1993.

[11]Lee-Rausch, E. M., and Batina, J. T., "Calculation of Agard Wing 445.6 Flutter using Navier-Stokes Aerodynamics," AIAA Paper No. 93–3476, Aug. 9-11 1993.

[12]Doggett, R. V. Jr., "Viscosity and Reynolds Number Effects on Transonic Flutter – Status Report," Aerospace Flutter and Dynamics Council Meeting, Scottsdale, AZ, May 5-6 1994.

[13]Batina, J. T., "Unsteady Transonic Small-Disturbance Theory Including Entropy and Vorticity Effects," *Journal of Aircraft*, vol. 26, pp. 531–538, June 1989.

[14]Keller, D. F., unpublished NASA Langley Transonic Dynamics Tunnel data, NASA Langley Research Center, 1993.

[15]Bennett, R. M., and Desmarais, R. N., "Curve Fitting of Aeroelastic Transient Response Data with Exponential Functions," Flutter Testing Techniques, NASA SP-415, May 1975.

[16]Zwann, R. J., "Aeroelastic Problems of Wings in Transonic Flow," NLR MP 81005U, National Aerospace Laboratory, Amsterdam, Feb. 1981.

[17]Mohr, R. W., Batina, J. T., and Yang, H. T. Y., "Mach number effects on transonic aeroelastic forces and flutter characteristics," AIAA Paper No. 88–2304, Apr. 18-20 1988.

Table 1 Wing mode shape information.

Mode Shape	Generalized Mass $(\frac{lb_f\,sec^2}{inch})$	Frequencies (Hz.)
1	0.0040196	4.30
2	0.0019749	14.50
3	0.0049215	31.60
4	0.0012095	33.00
5	0.0018510	58.20
6	0.00060438	62.66

Table 2 Effects of number of time steps per cycle of motion on the dynamic pressure and frequency at flutter computed with CAP-TSD using the linear equation at M_∞=0.9.

steps/cycle	165	330	660
dynamic pressure (psf)	91.38	85.23	84.25
frequency (Hz)	9.37	8.82	8.74

Table 3 Effects of generalized velocity initial conditions on the damping and frequency content of the first generalized displacement computed with CAP-TSD using the nonlinear equation at M_∞=0.85 and q_∞=64.8 psf.

	$\dot{q}_i$ = 0.1	$\dot{q}_i$ = 1.0	$\dot{q}_i$ = 10.0
damping	-0.00477	-0.00466	-0.00454
frequency	7.972	7.971	7.975

Table 4 Effects of generalized velocity initial conditions on the damping and frequency content of the first generalized displacement computed with CAP-TSD using the nonlinear equation at M_∞=0.90 and q_∞=21.6 psf.

	$\dot{q}_i$ = 1.0	$\dot{q}_i$ = 10.0
damping	-0.0117	-0.0118
frequency	5.603	5.602

Table 5 Experimental flutter data for the business jet wing obtained in air in the NASA Langley Research Center Transonic Dynamics Tunnel.

Mach No.	Velocity (ft/sec)	Dynamic Pressure (psf)	Density (Slug/ft^3) 10^{-4}	Freq. (Hz)	Reduced Freq.	Mass Ratio
0.628	708.1	148.3	5.91	13.1	0.110	184.1
0.698	781.0	140.6	4.61	12.5	0.095	236.0
0.781	863.2	125.3	3.36	11.3	0.078	323.8
0.844	929.2	109.5	2.54	10.4	0.067	428.4
0.888	971.2	106.8	2.26	9.3	0.057	481.5

Table 6 CAP–TSD flutter results computed using the linear equation for the wing/fuselage configuration.

Mach No.	Velocity (ft/sec)	Dynamic Pressure (psf)	Density (Slug/ft^3) 10^{-4}	Freq. (Hz)	Reduced Freq.	Mass Ratio	Flutter Speed Index
0.600	669.6	146.04	6.51435	12.96	0.1152	167.03	0.2755
0.700	781.2	134.57	4.41015	12.08	0.0920	246.73	0.2645
0.800	880.0	117.23	3.02763	10.83	0.0732	359.40	0.2468
0.850	935.0	104.03	2.37990	9.98	0.0635	457.21	0.2325
0.900	990.0	85.23	1.73921	8.82	0.0530	625.63	0.2105
0.980	1078.0	31.80	0.54729	5.92	0.0327	1988.2	0.1286
1.050	1155.0	91.33	1.36924	9.21	0.0475	794.7	0.2176

Table 7 CAP-TSD flutter results computed using the nonlinear equation for the wing/fuselage configuration.

Mach No.	Velocity (ft/sec)	Dynamic Pressure (psf)	Density (Slug/ft^3) 10^{-4}	Freq. (Hz)	Reduced Freq.	Mass Ratio	Flutter Speed Index
0.600	669.6	142.4	6.35198	12.74	0.1132	171.30	0.2720
0.700	781.2	124.1	4.06703	11.60	0.0884	267.54	0.2540
0.800	880.0	91.1	2.35279	9.45	0.0639	462.48	0.2176
0.850	935.0	59.7	1.36578	7.63	0.0486	796.70	0.1761
0.950	1045.0	284.42	5.20904	15.56	0.0886	208.89	0.3845
1.05	1155.0	358.00	5.36722	16.24	0.0837	202.73	0.4313

Table 8 CAP-TSD flutter results computed using the nonlinear equation for the extended wing configuration.

Mach No.	Velocity (ft/sec)	Dynamic Pressure (psf)	Density (Slug/ft^3) 10^{-4}	Freq. (Hz)	Reduced Freq.	Mass Ratio	Flutter Speed Index
0.700	781.2	126.0	4.12930	11.62	0.0885	263.51	0.2559
0.800	880.0	98.1	2.53357	9.93	0.0671	429.5	0.2258
0.850	935.0	63.9	1.46187	7.85	0.0500	744.33	0.1822

Table 9 CAP-TSD flutter results computed using the nonlinear equation by varying U for the wing/fuselage configuration.

Mach No.	Velocity (ft/sec)	Dynamic Pressure (psf)	Density (Slug/ft^3) 10^{-4}	Freq. (Hz)	Reduced Freq.	Mass Ratio	Flutter Speed Index
0.800	771.3	93.0	3.12140	9.60	0.0741	348.60	0.2196
0.900	559.5	34.2	2.18364	6.21	0.0660	498.30	0.1333

Table 10 CAP-TSD flutter results computed using the nonlinear equation for different mass ratios with the wing/fuselage configuration.

Mach No.	Velocity (ft/sec)	Dynamic Pressure (psf)	Density (Slug/ft^3) 10^{-4}	Freq. (Hz)	Reduced Freq.	Mass Ratio	Flutter Speed Index
0.900	646.0	113.54	5.44056	28.48	0.2623	200.00	0.2429
0.900	559.5	34.2	2.18364	6.21	0.0660	498.30	0.1333

Table 11 CFL3D–Euler flutter results computed for the extended wing configuration.

Mach No.	Velocity (ft/sec)	Dynamic Pressure (psf)	Density (Slug/ft^3) 10^{-4}	Freq. (Hz)	Reduced Freq.	Mass Ratio	Flutter Speed Index
0.700	781.2	118.1	3.87040	11.81	0.0900	281.14	0.2477
0.850	935.0	69.1	1.58083	8.62	0.0549	688.3	0.1895
0.900	990.0	32.83	0.66993	6.24	0.0375	1624.2	0.1306
1.050	1155.0	266.2	3.99020	20.77	0.1070	272.7	0.3719

Table 12 CFL3D-Euler flutter results computed for different mass ratios with the extended wing configuration.

Mach No.	Velocity (ft/sec)	Dynamic Pressure (psf)	Density (Slug/ft^3) 10^{-4}	Freq. (Hz)	Reduced Freq.	Mass Ratio	Flutter Speed Index
0.850	760.0	72.2	2.50185	8.81	0.0690	434.9	0.1937
0.900	667.0	48.6	2.18364	7.07	0.0632	498.30	0.1583

Table 13 CFL3D-Navier–Stokes flutter results computed with the extended wing configuration.

Mach No.	Velocity (ft/sec)	Dynamic Pressure (psf)	Density (Slug/ft^3) 10^{-4}	Freq. (Hz)	Reduced Freq.	Mass Ratio	Flutter Speed Index
0.850	935.0	80.4	1.83866	8.80	0.0560	591.8	0.2044
0.900	990.0	79.8	1.62881	8.16	0.0491	668.0	0.2037
0.920	1012.0	111.7	2.18133	9.10	0.0535	498.8	0.2410

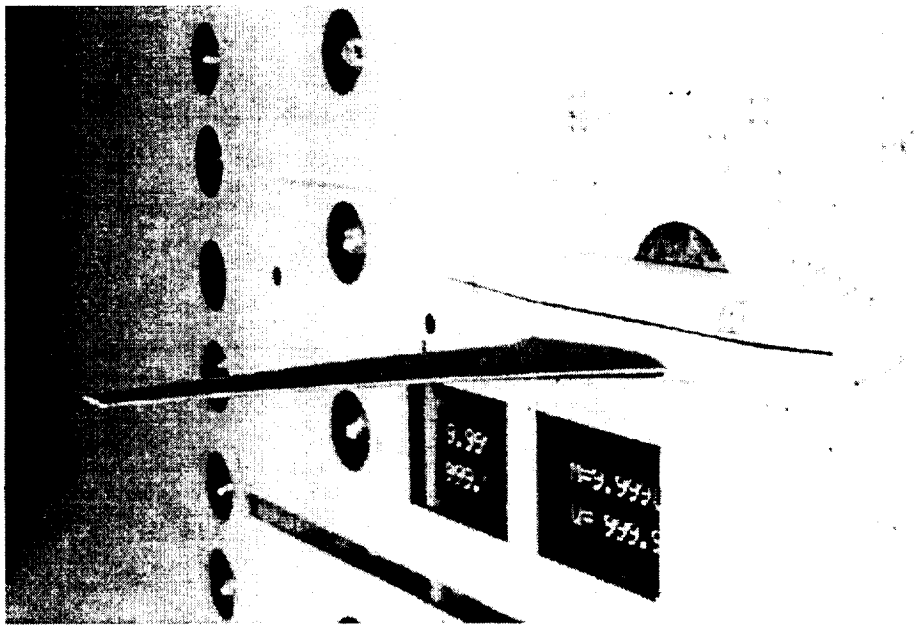

Figure 1 Semispan business jet model mounted in the NASA Langley Research Center Transonic Dynamics Tunnel.

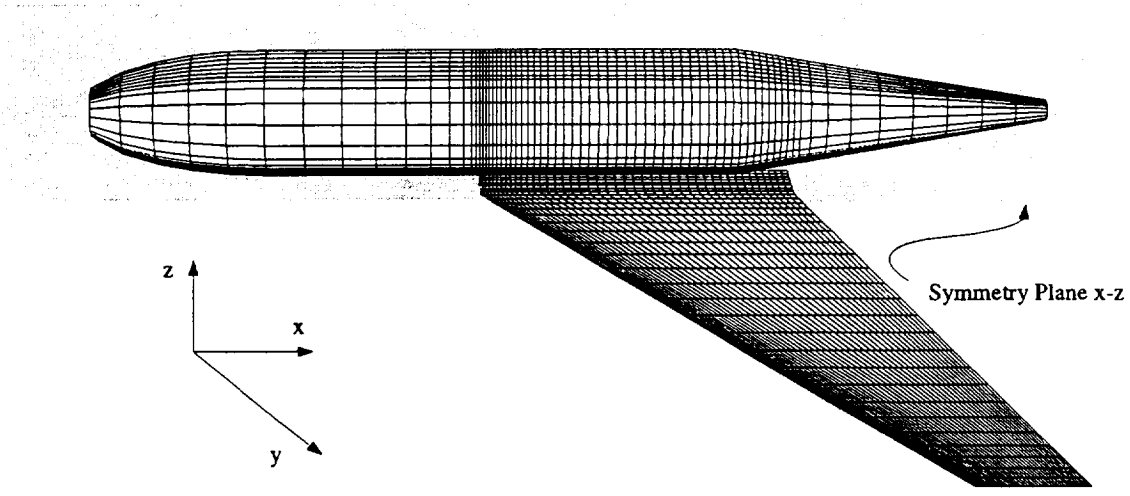

Figure 2 Wing/fuselage surface grid used with CAP-TSD calculations.

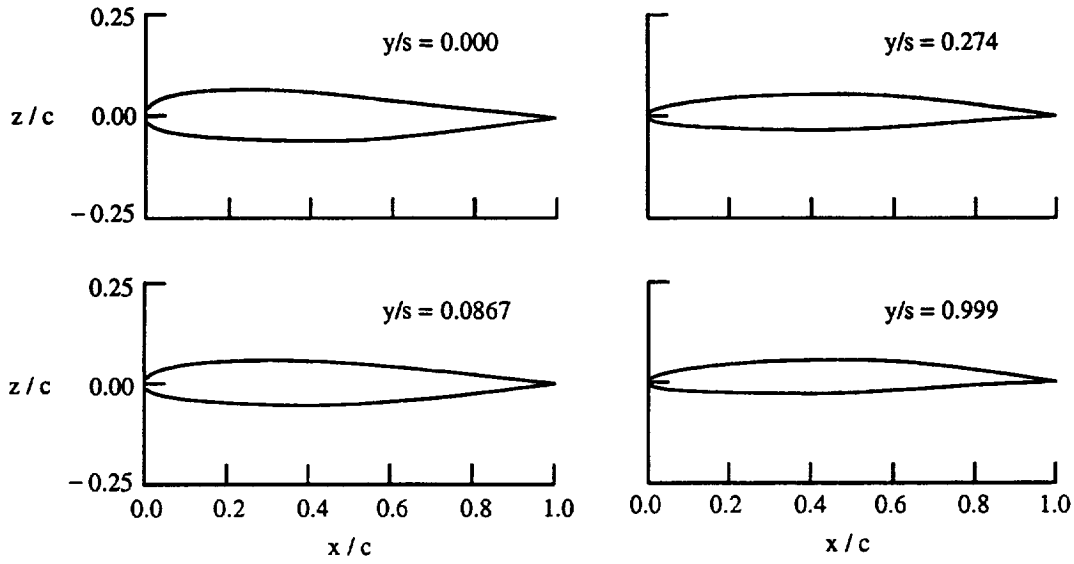

Figure 3 Airfoil sections at symmetry plane, 8.67, 27.4 and 99.9 percent span.

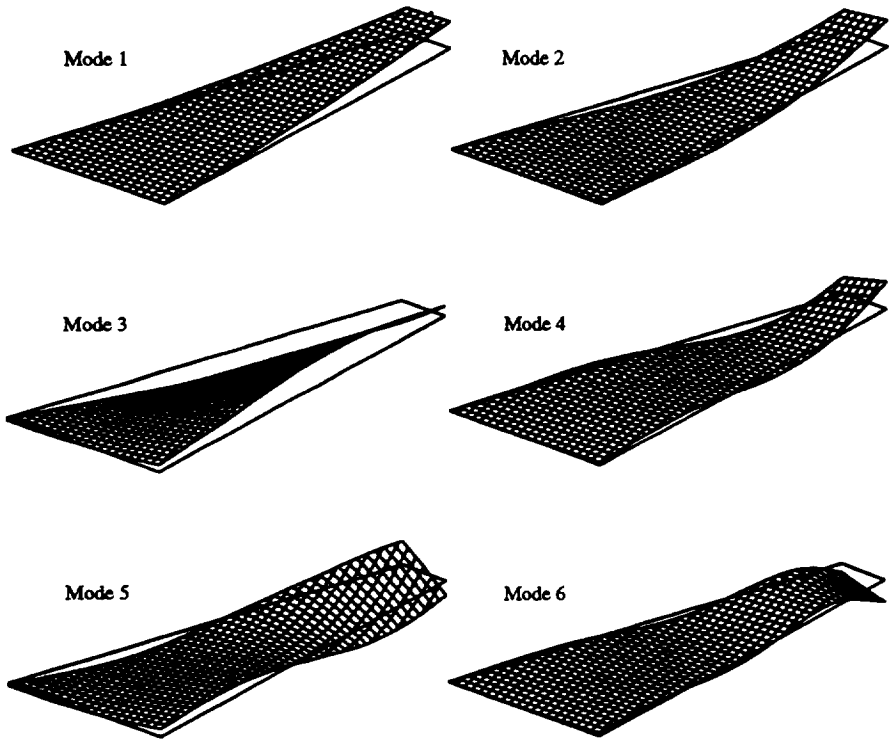

Figure 4 Wing mode shapes of the 6 modes used for aeroelastic analysis.

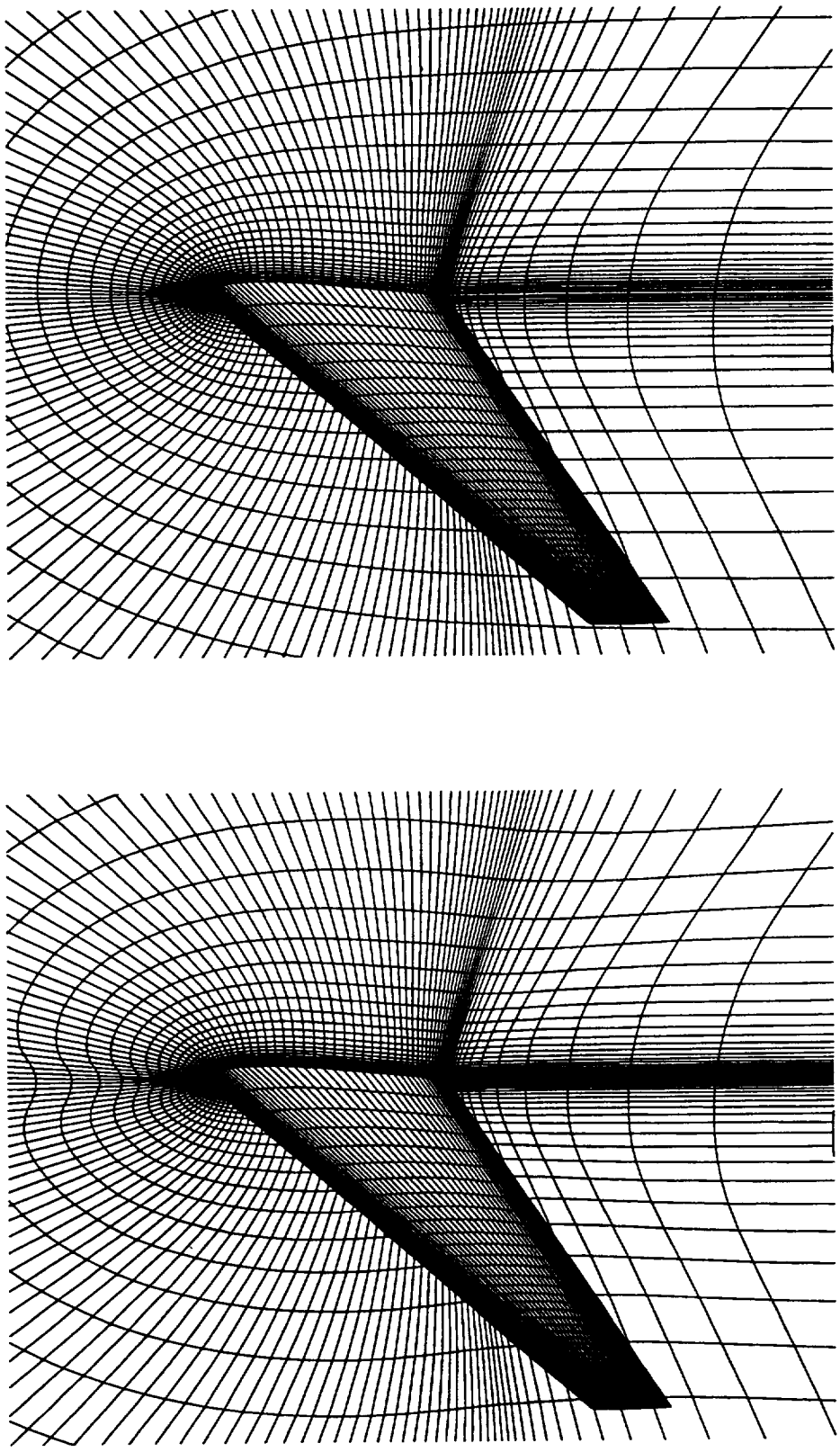

Figure 6 Symmetry plane and wing surface grid used for CFL3D Navier-Stokes calculations.

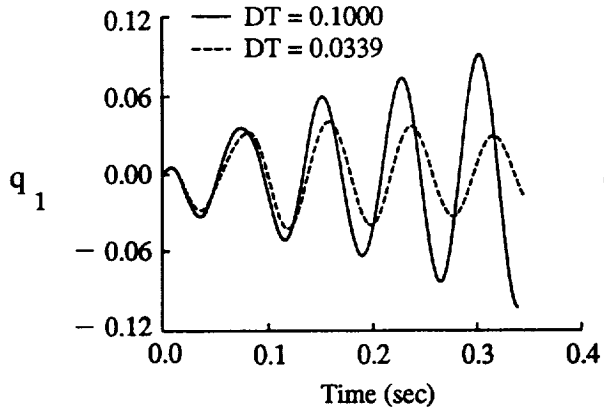

Figure 7 Effects of time step on the first generalized displacement computed with CAP-TSD using the nonlinear equation at M_∞=0.6 and q_∞=136.8 psf.

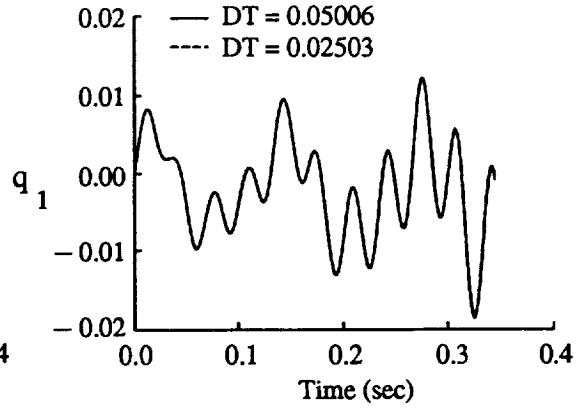

Figure 8 Effects of time step on the first generalized displacement computed with CAP-TSD using the nonlinear equation at M_∞=0.9 and q_∞=57.6 psf.

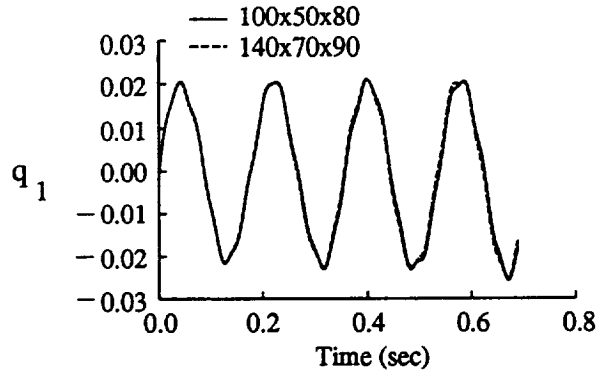

Figure 9 Effects of grid density on the first generalized displacement computed using CAP-TSD with the nonlinear equation at M_∞=0.9 and q_∞=21.6 psf.

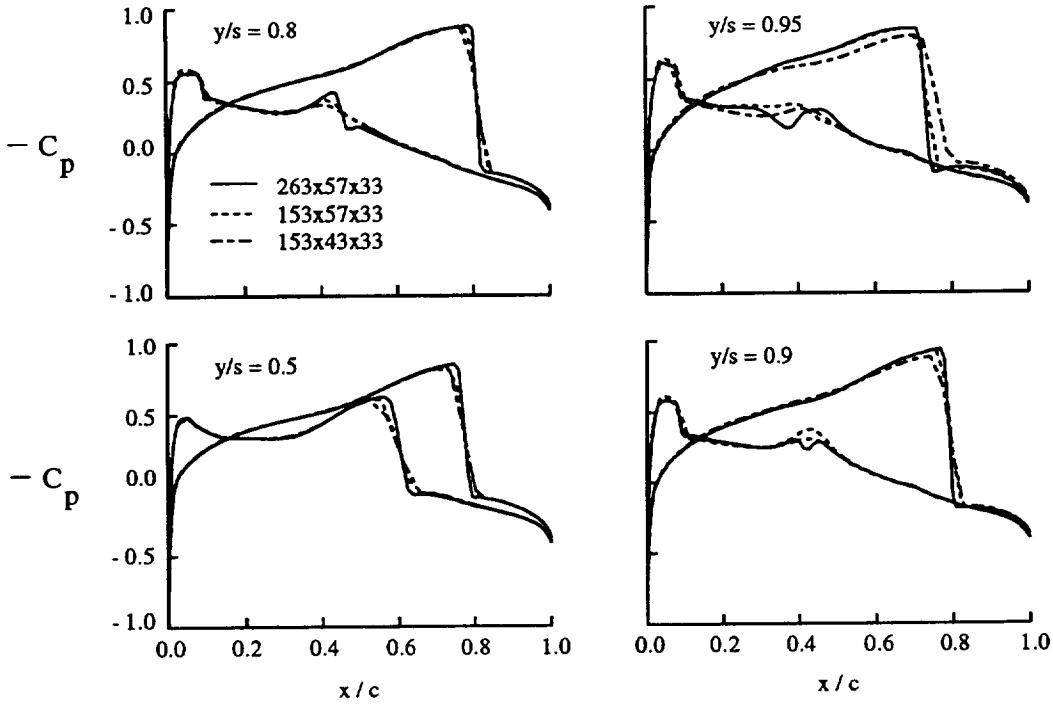

Figure 10 Effects of grid density on steady pressure coefficients computed using CFL3D-Euler results at M_∞=0.9 and α = 0 for a rigid case.

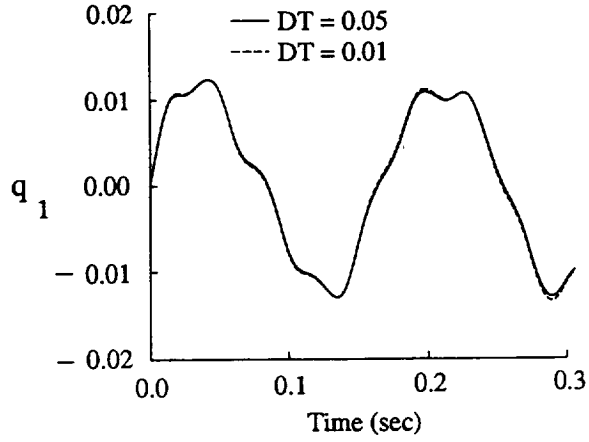

Figure 11 Effects of time step on the first generalized displacement computed using CFL3D-Euler at M_∞=0.9 and q_∞=36.0 psf.

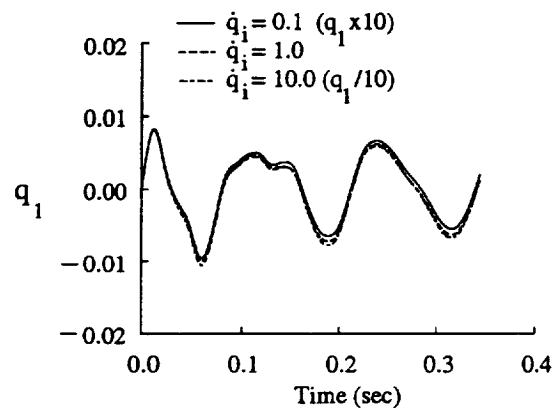

Figure 12 Effect of generalized velocity initial conditions on the first generalized displacement computed with CAP-TSD using the nonlinear equation at M_∞=0.85 and q_∞=64.8 psf.

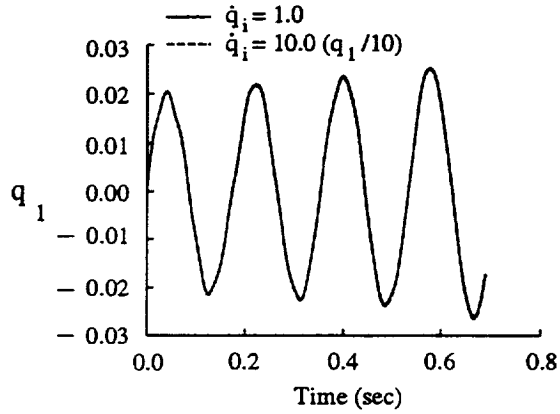

Figure 13 Effect of generalized velocity initial conditions on the first generalized displacement computed with CAP-TSD using the nonlinear equation at M_∞=0.90 and q_∞=21.6 psf.

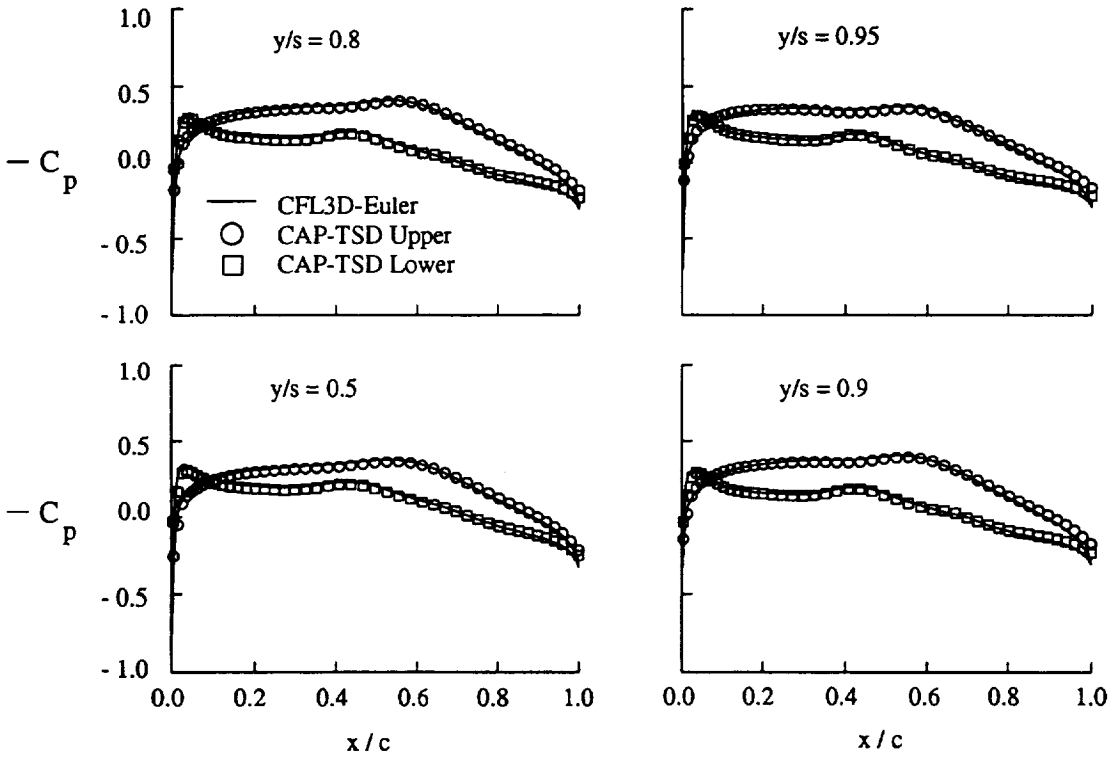

Figure 14 Comparison of CAP-TSD and CFL3D-Euler steady pressure coefficients for the extended rigid wing configuration at M_∞=0.7 and α = 0.

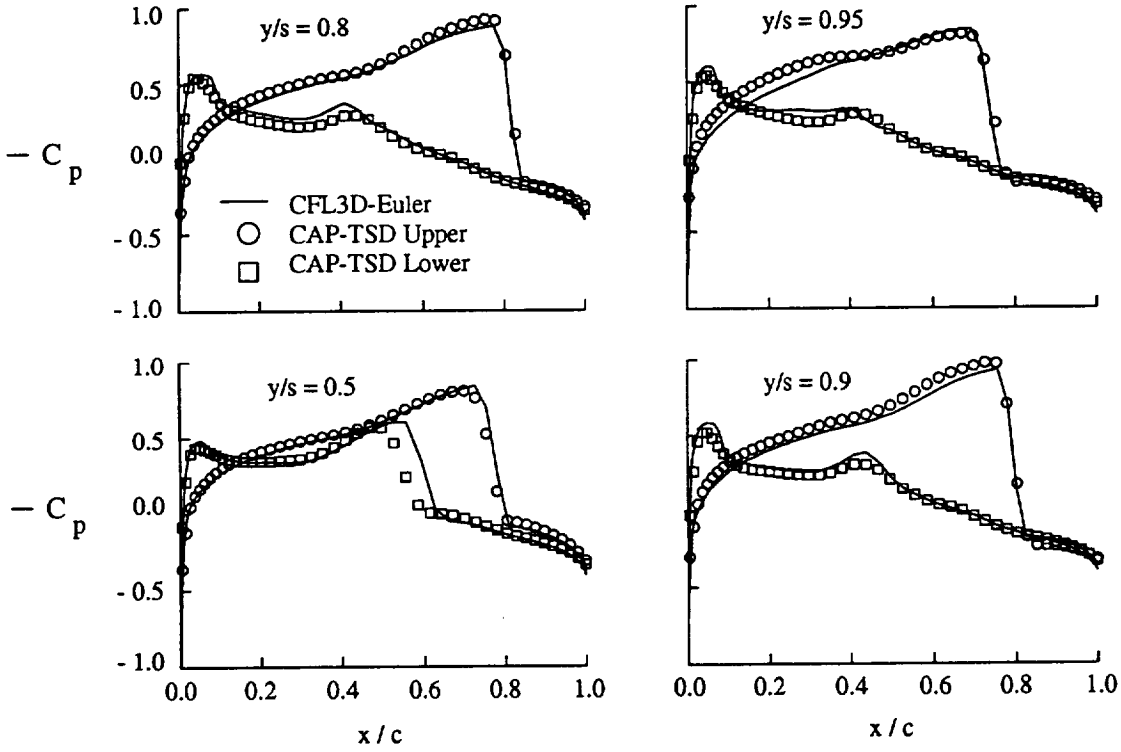

Figure 15 Comparison of CAP-TSD and CFL3D-Euler steady pressure coefficients for the extended rigid wing configuration at M_∞=0.9 and $\alpha = 0$.

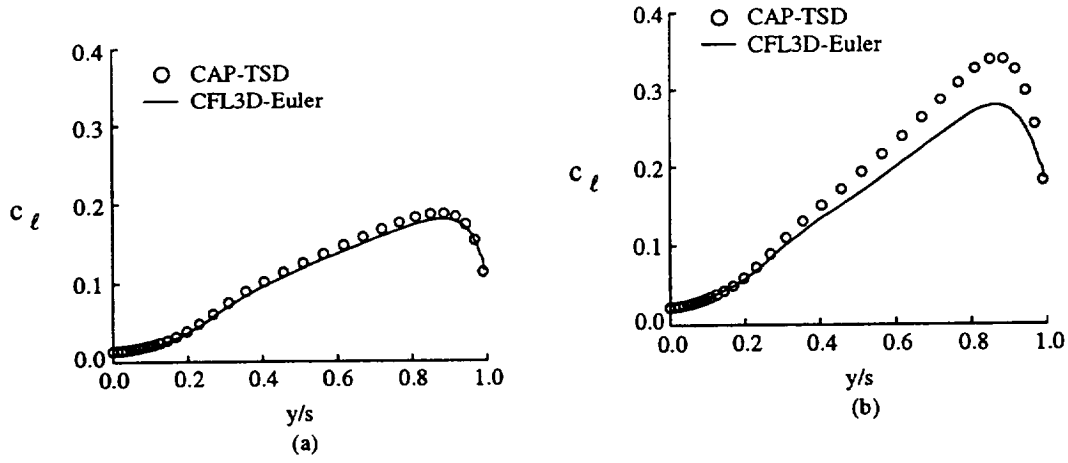

Figure 16 Comparison of sectional lift coefficients computed using CAP-TSD and CFL3D-Euler for the steady rigid case at (a) M_∞=0.7, $\alpha = 0$ and (b) M_∞=0.9, $\alpha = 0$.

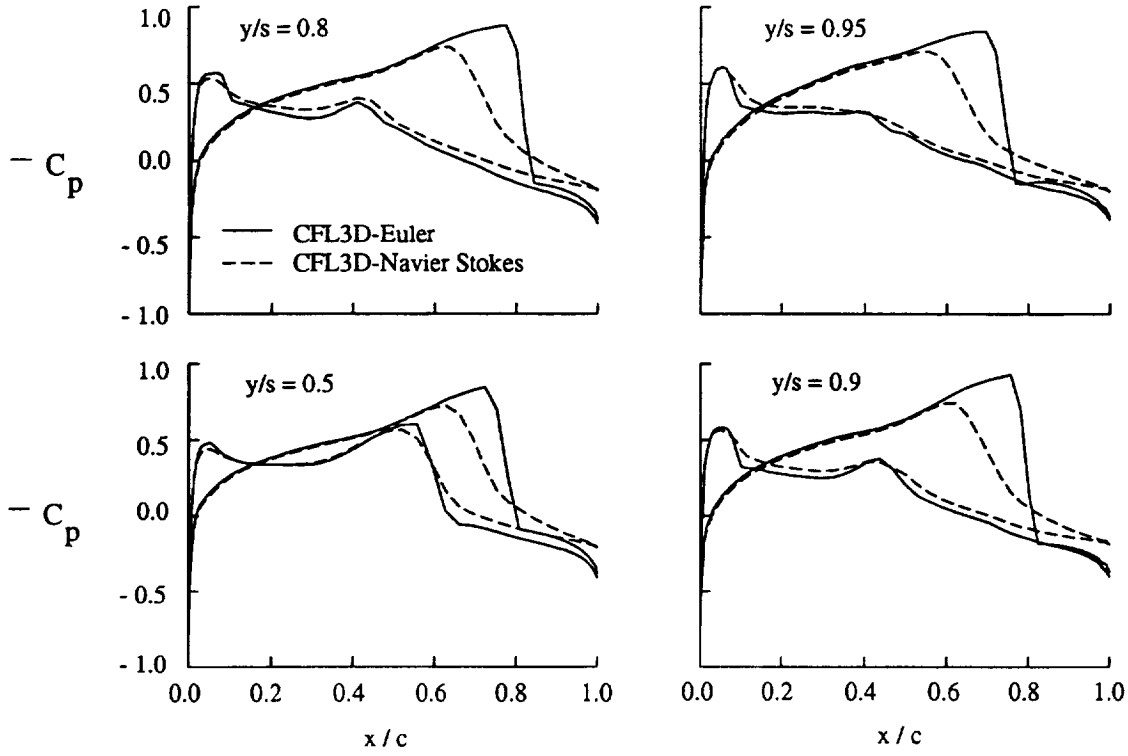

Figure 17 Comparison of CFL3D-Euler and CFL3D-Navier-Stokes steady pressure coefficients for the rigid extended wing configuration at M_∞=0.9, α = 0, Re = 1.107x10^6.

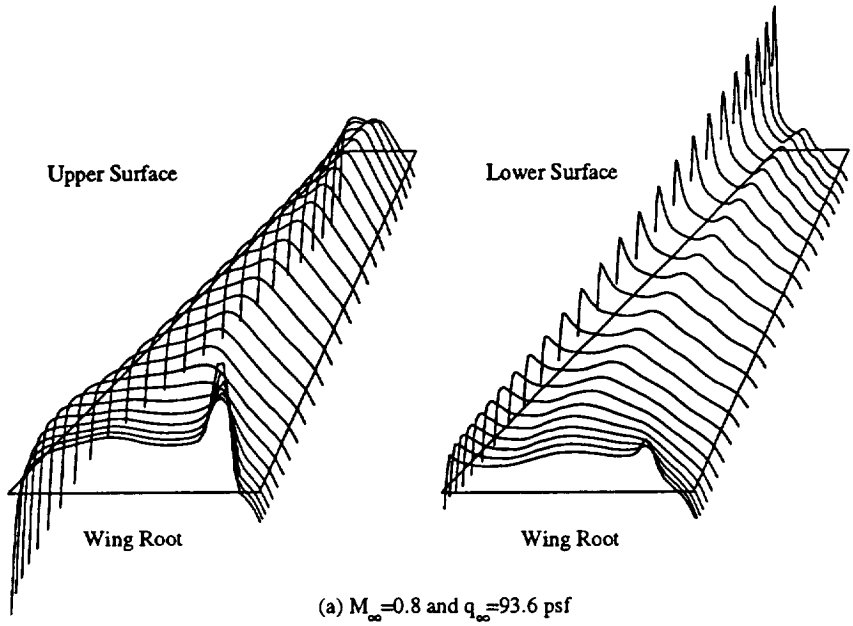

(a) M_∞=0.8 and q_∞=93.6 psf

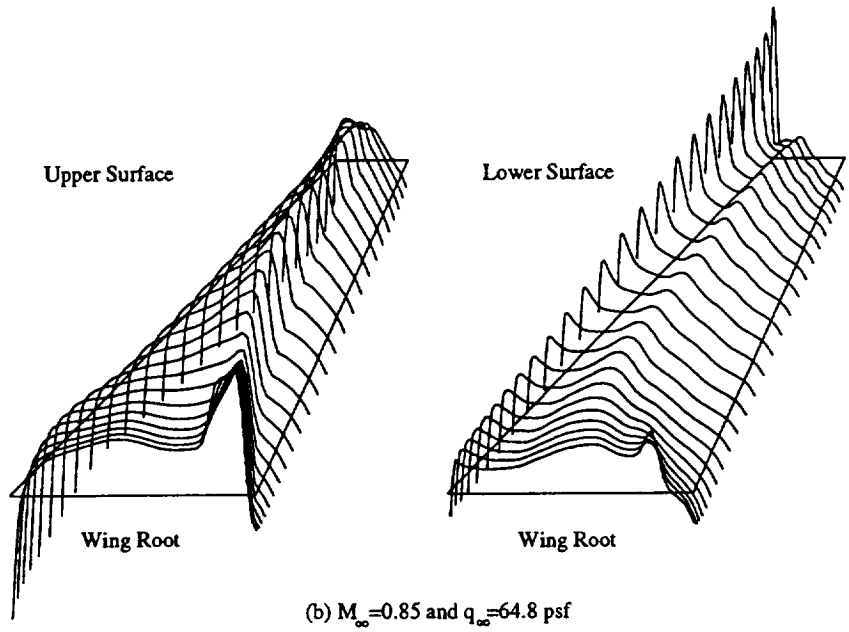

(b) M_∞=0.85 and q_∞=64.8 psf

Figure 18 Effects of freestream Mach number (and dynamic pressure) on steady pressure coefficients computed using CAP-TSD for the wing/fuselage configuration under static aeroelastic deformation with dynamic pressure near the flutter value.

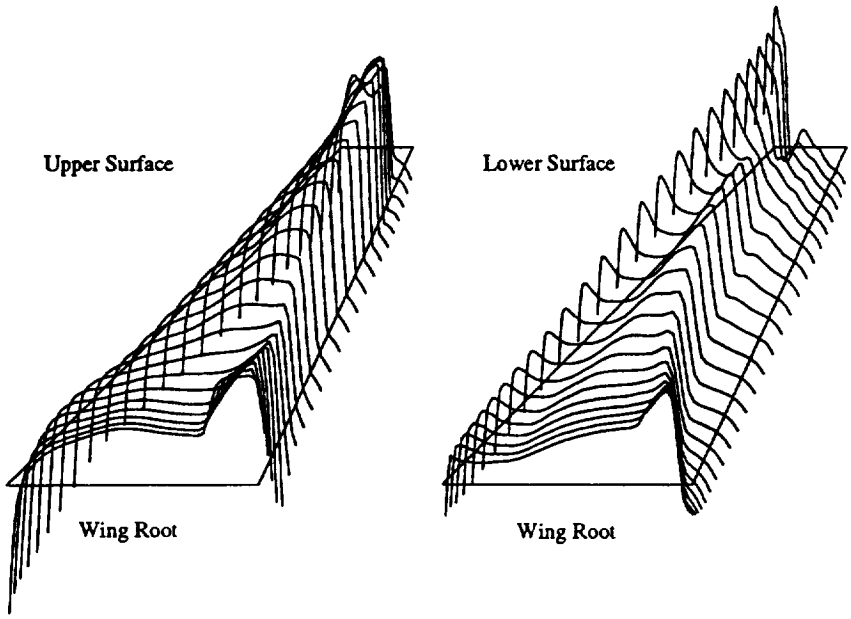

(c) M_∞=0.90 and q_∞=21.6 psf.

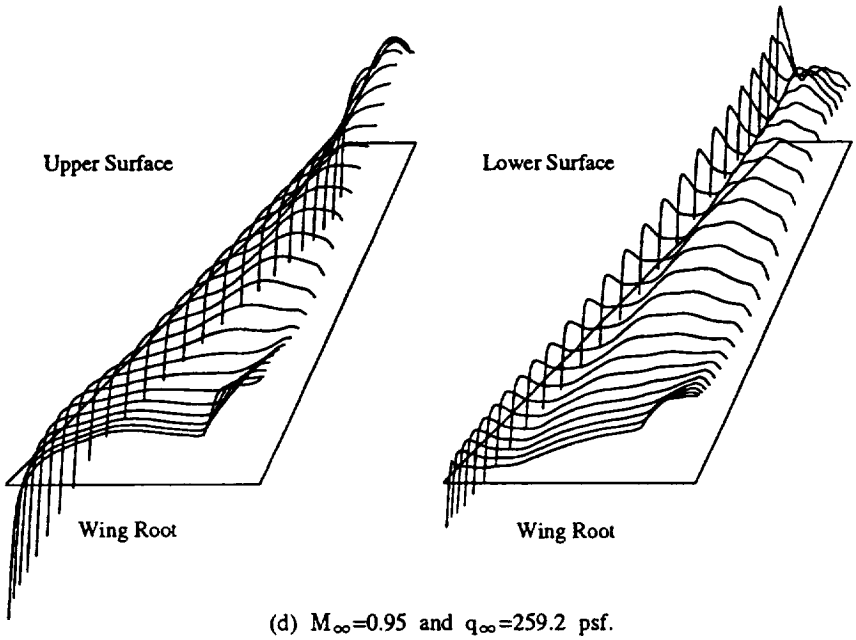

(d) M_∞=0.95 and q_∞=259.2 psf.

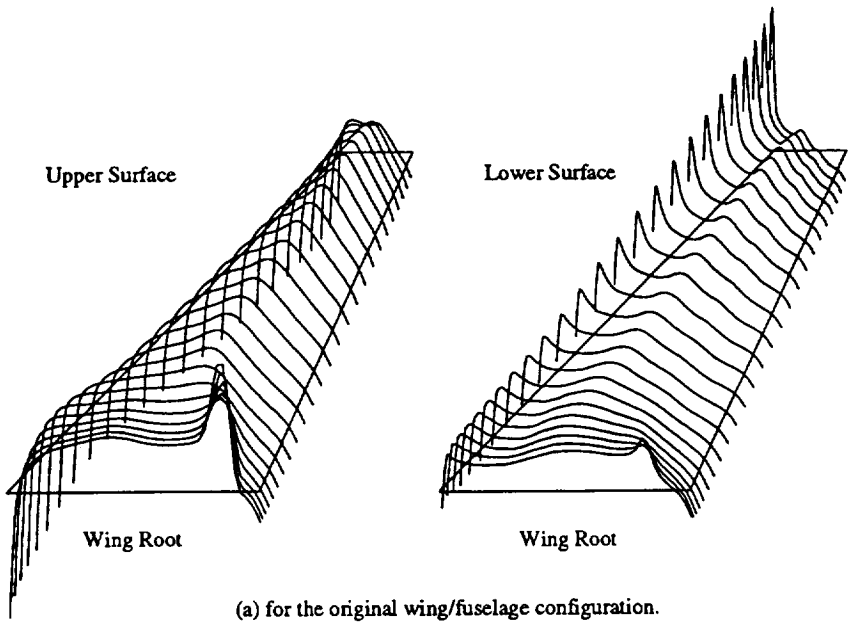

(a) for the original wing/fuselage configuration.

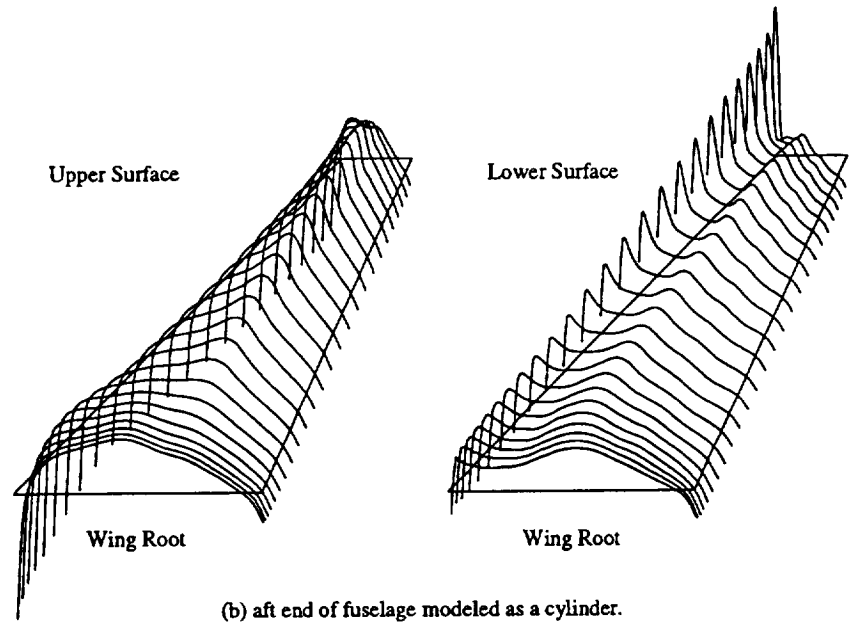

(b) aft end of fuselage modeled as a cylinder.

Figure 18 Effects of fuselage modeling on steady pressure coefficients computed using CAP-TSD at M=0.85 and q=64.8 psf.

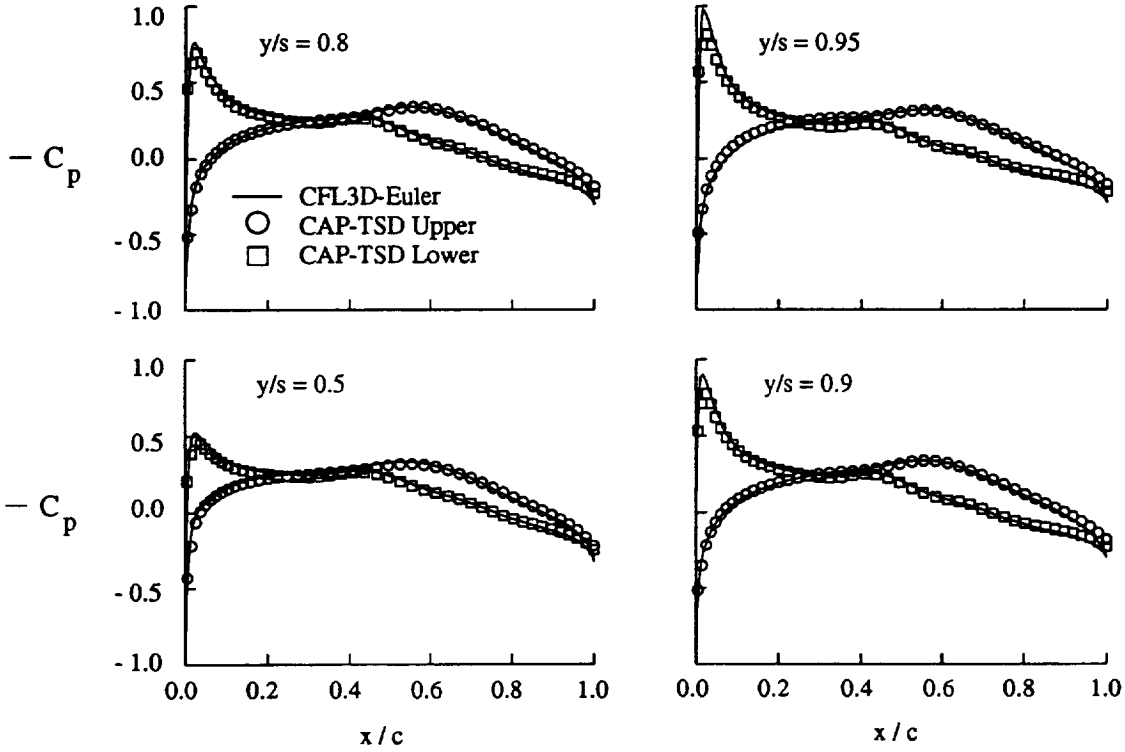

Figure 19 Comparison of CAP-TSD and CFL3D-Euler steady pressure coefficients for the extended wing configuration with static aeroelastic deflection at M_∞=0.7 and q_∞=115.2 psf.

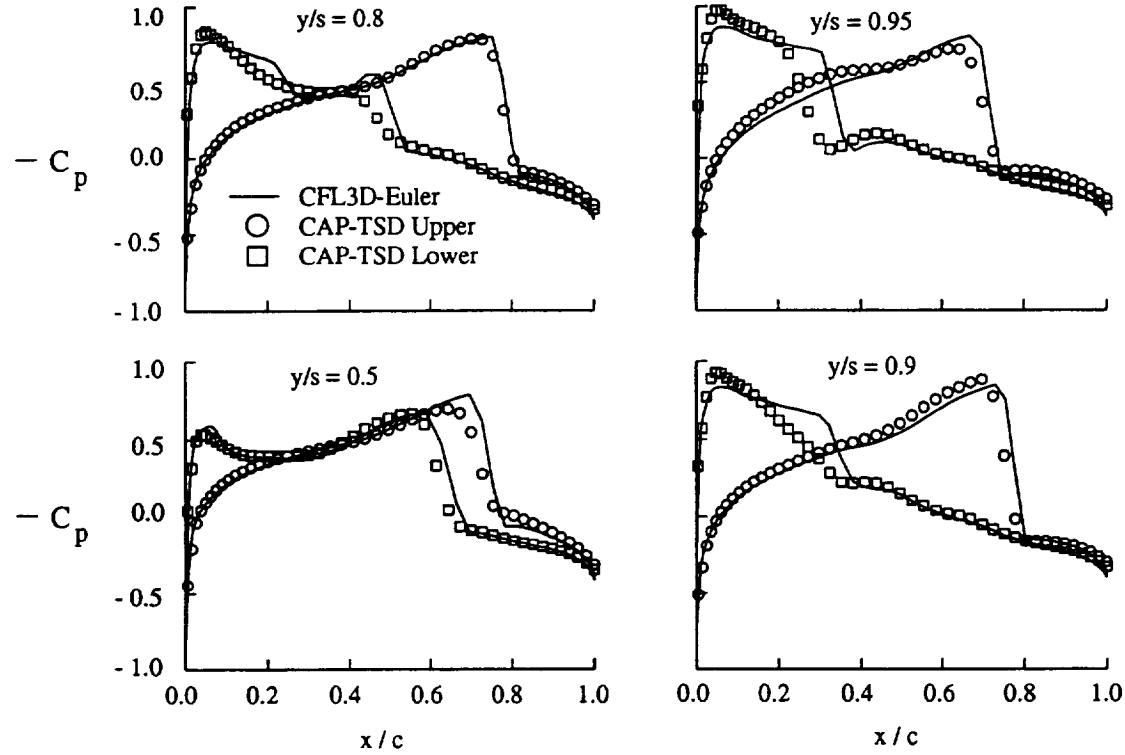

Figure 20 Comparison of CAP-TSD and CFL3D-Euler steady pressure coefficients for the extended wing configuration with static aeroelastic deformation at M_∞=0.9 and q_∞=36.0 psf.

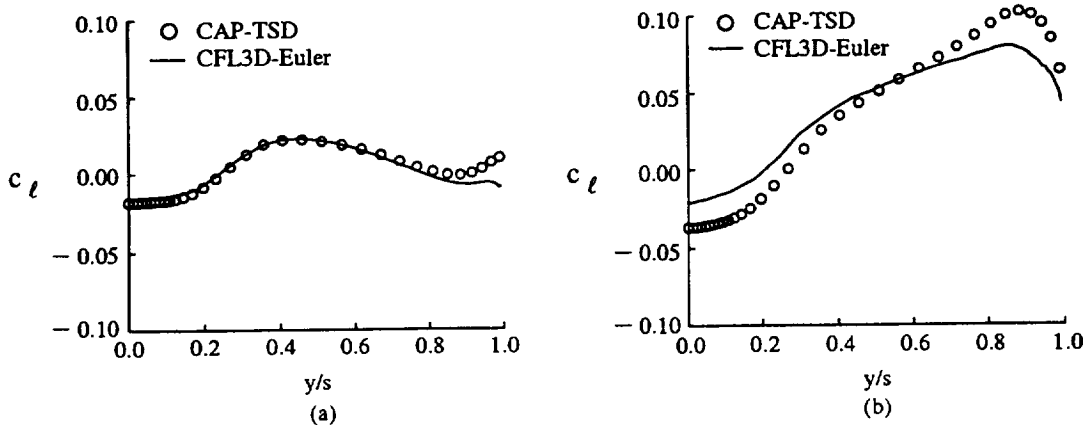

Figure 21 Comparison of sectional lift coefficients computed using CAP-TSD and CFL3D-Euler for static aeroelastic cases at (a) M_∞=0.7, q_∞=115.2 psf and (b) M_∞=0.9, q_∞=36.0 psf.

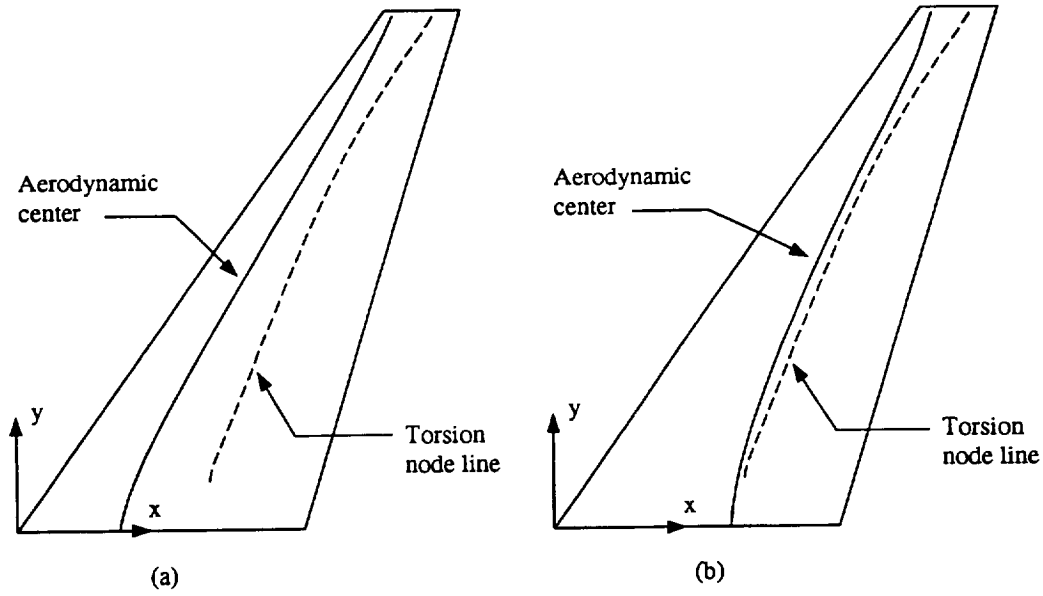

Figure 22 Aerodynamic center location in relation to the first torsion node line computed using CAP-TSD for static aeroelastic cases at (a) M_∞=0.7, q_∞=115.2 psf and (b) M_∞=0.9, q_∞=36.0 psf.

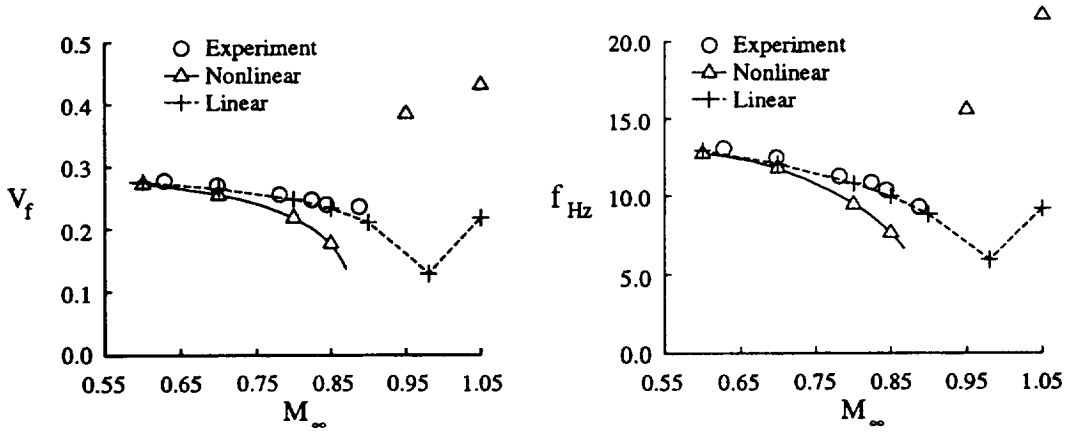

Figure 23 CAP-TSD flutter points computed using the linear and nonlinear equations compared with Experimental data for the wing/fuselage configuration.

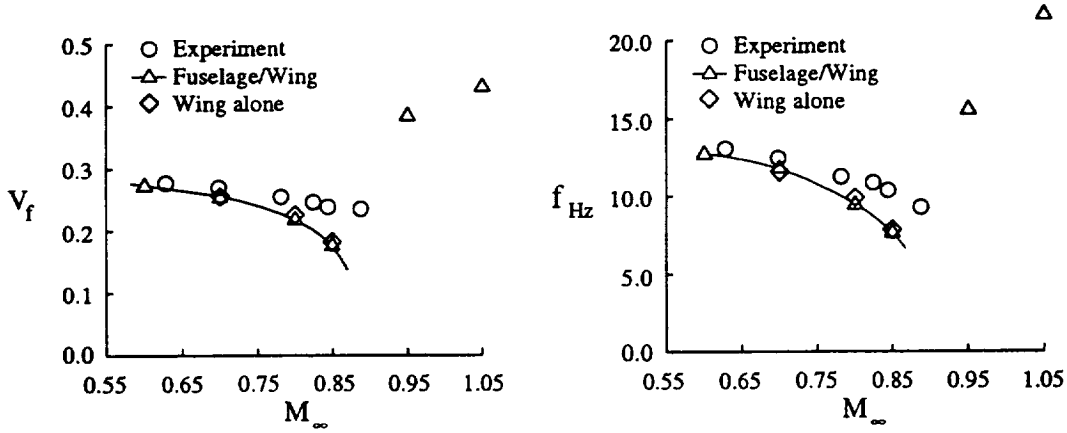

Figure 24 Effects of fuselage modeling on the predicted flutter boundary using the nonlinear CAP-TSD equation.

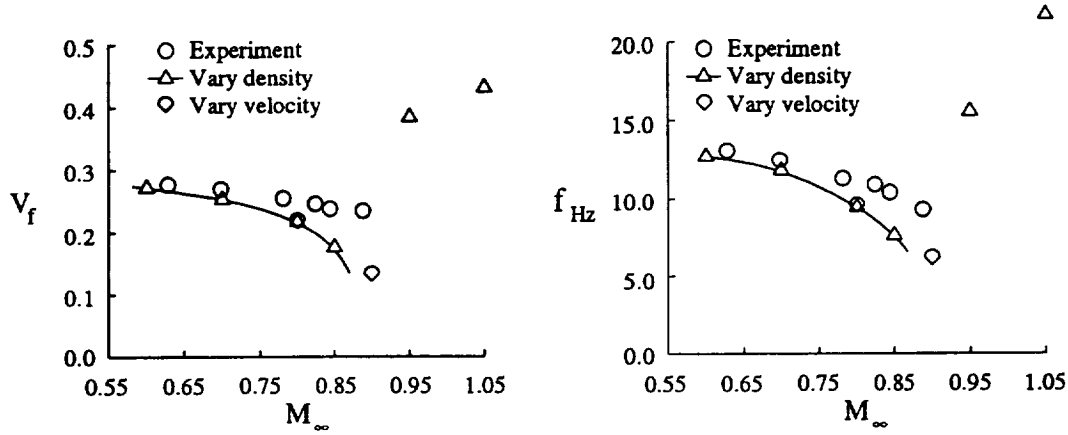

Figure 25 Effects of mass ratio on the predicted flutter boundary using the nonlinear CAP-TSD equation for the wing/fuselage configura

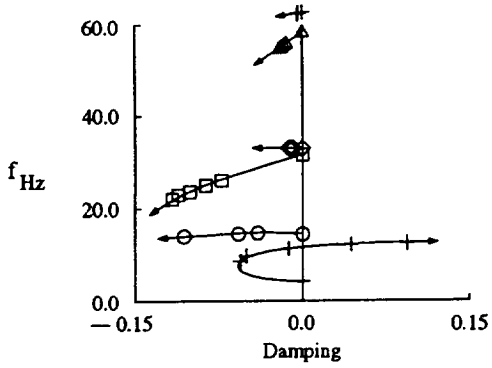

(a) M_∞=0.7

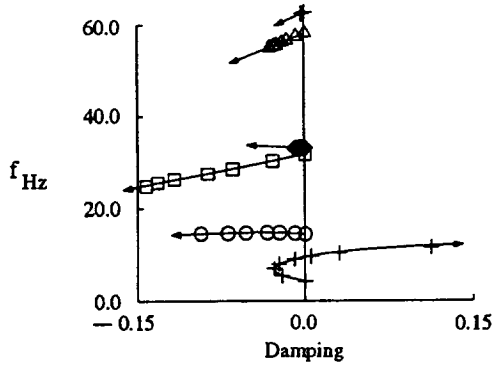

(b) M_∞=0.8

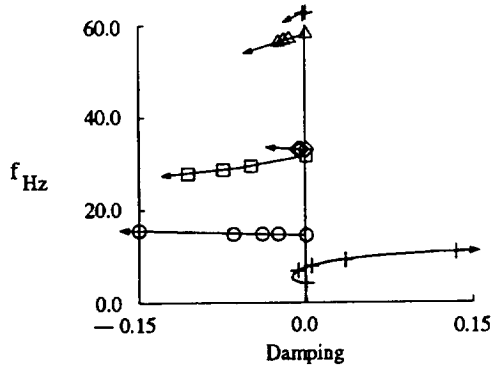

(c) M_∞=0.85

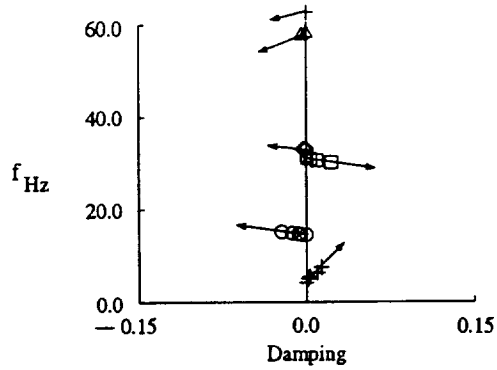

(d) M_∞=0.9

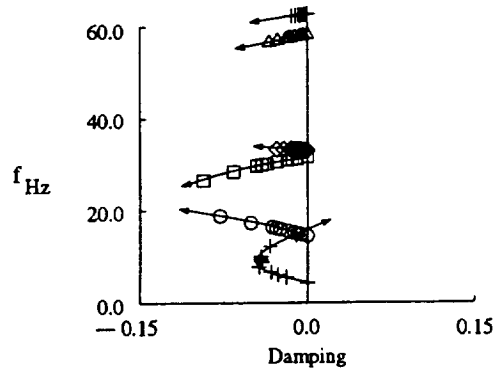

(e) M_∞=0.95

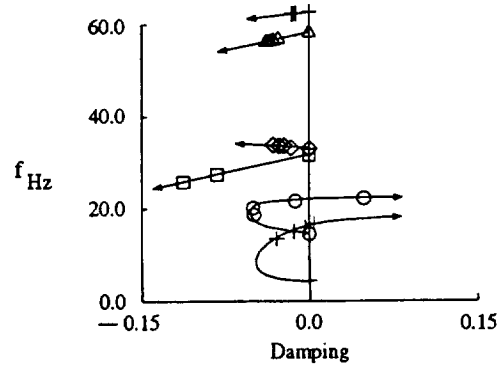

(f) M_∞=1.05

Figure 26 Effects of freestream Mach number on aeroelastic stability computed using CAP-TSD with the nonlinear equation varying density as a parameter.

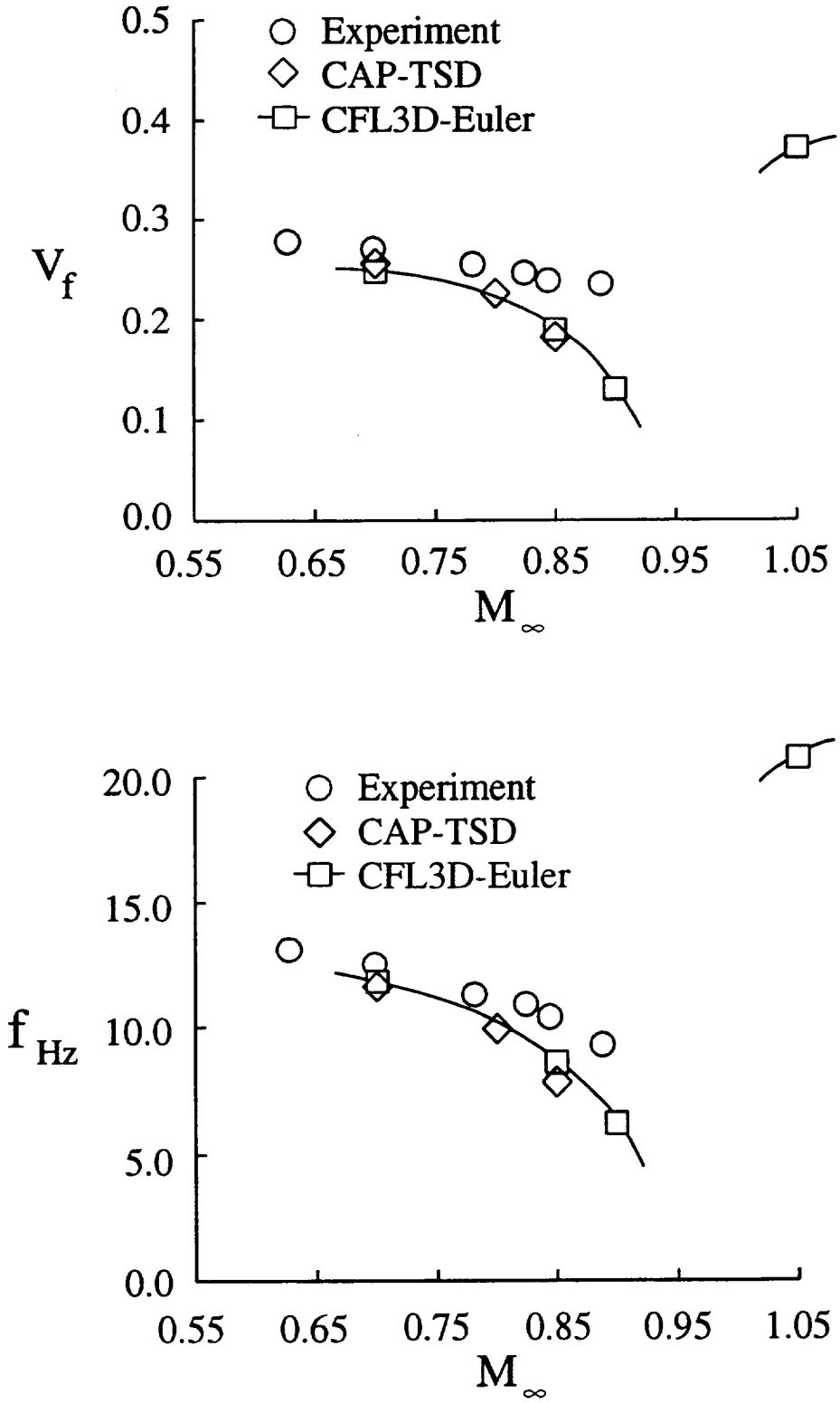

Figure 27 Comparison of CFL3D-Euler and CAP-TSD computed flutter solutions with experimental data for the extended wing configuration.

REPORT DOCUMENTATION PAGE

Form Approved
OMB No. 0704-0188

1. AGENCY USE ONLY *(Leave blank)*	2. REPORT DATE	3. REPORT TYPE AND DATES COVERED
	September 1996	Contractor Report

4. TITLE AND SUBTITLE
Aeroelastic Calculations Using CFD for a Typical Business Jet Model

5. FUNDING NUMBERS
C NAS1-19000
WU 505-63-50-13

6. AUTHOR(S)
Michael D. Gibbons

7. PERFORMING ORGANIZATION NAME(S) AND ADDRESS(ES)
Lockheed Martin Engineering and Sciences Company
144 Research Drive
Hampton, VA 23666

8. PERFORMING ORGANIZATION REPORT NUMBER

9. SPONSORING / MONITORING AGENCY NAME(S) AND ADDRESS(ES)
NASA Langley Research Center
Hampton, VA 23681-0001

10. SPONSORING / MONITORING AGENCY REPORT NUMBER
NASA CR-4753

11. SUPPLEMENTARY NOTES
NASA Langley technical monitor: Thomas E. Noll

12a. DISTRIBUTION / AVAILABILITY STATEMENT
Unclassified—Unlimited

Subject Category 05

12b. DISTRIBUTION CODE

13. ABSTRACT ***(Maximum 200 words)***

Two time–accurate Computational Fluid Dynamics (CFD) codes were used to compute several flutter points for a typical business jet model. The model consisted of a rigid fuselage with a flexible semispan wing and was tested in the Transonic Dynamics Tunnel at NASA Langley Research Center where experimental flutter data were obtained from M_∞=0.628 to M_∞=0.888. The computational results were computed using CFD codes based on the inviscid TSD equation (CAP–TSD) and the Euler/Navier–Stokes equations (CFL3D–AE). Comparisons are made between analytical results and with experiment where appropriate. The results presented here show that the Navier–Stokes method is required near the transonic dip due to the strong viscous effects while the TSD and Euler methods used here provide good results at the lower Mach numbers.

14. SUBJECT TERMS
Computational aeroelasticity, flutter, transonic flow, transonic small disturbance aerodynamics, Euler/Navier–Stokes aerodynamics

15. NUMBER OF PAGES
45

16. PRICE CODE
A03

17. SECURITY CLASSIFICATION OF REPORT	18. SECURITY CLASSIFICATION OF THIS PAGE	19. SECURITY CLASSIFICATION OF ABSTRACT	20. LIMITATION OF ABSTRACT
Unclassified	Unclassified	Unclassified	